Optical Engineering

OpticalEngineering.SPIEDigitalLibrary.org

Principles of surface-phase-resolved shearography

Michael J. DeWeert
Andrew N. Acker
Reid Noguchi
Dugan Yoon
Gary Sawai

SPIE.

Michael J. DeWeert, Andrew N. Acker, Reid Noguchi, Dugan Yoon, Gary Sawai, "Principles of surface-phase-resolved shearography," *Opt. Eng.* **58**(11), 114103 (2019), doi: 10.1117/1.OE.58.11.114103.

Optical Engineering 58(11), 114103 (November 2019)

Principles of surface-phase-resolved shearography

Michael J. DeWeert,* Andrew N. Acker, Reid Noguchi, Dugan Yoon, and Gary Sawai
BAE Systems Inc., Electronic Solutions Survivability, Targeting, and Sensing, Honolulu, Hawaii, United States

Abstract. There is a need to remotely measure the full phase and amplitude information of small-scale acousto-seismic vibrations in order to detect the presence of buried objects (e.g., tunnels, etc.), or for other purposes. This remote sensing information may need to be collected with a large area coverage rate and at a safe standoff distance. To accomplish this, we have implemented a shearographic imaging system that incorporates phase stepping in a novel way, automatically separating random speckle noise from surface motion, without requiring an intermediate unwrapping step. This method, which we call surface-phase-resolved shearography, is especially effective for very low-amplitude motions that generate less than one light-wavelength of phase change. In laboratory studies, we have demonstrated sensitivity of two nanometers RMS with 532-nm-wavelength light.
[DOI: 10.1117/1.OE.58.11.114103]

Keywords: imaging interferometry; lidar; remote sensing; vibrometry; shearography.

Paper 190858 received Jun. 25, 2019; accepted for publication Oct. 10, 2019; published online Nov. 12, 2019.

1 Introduction

In conventional nonphase-resolved (NPR) shearography, the variations in the image intensity and contrast (due to surface variations or beam inhomogeneity) add noise that must be mitigated by algorithms to maximize the speckle contrast. Current state-of-the-art phase-stepped (PS) shearography separates optical phase, composed of random speckle and signals of interest, from the variations in intensity and contrast, producing clearer fringes. However, even with phase stepping, shearographic fringes are dominated by random speckle-to-speckle phase variations. This random speckle-phase noise consumes dynamic range and adds significant processing burden to derive clear continuous fringes. Further, the random speckle phases obscure the direction (up or down) of the surface motion so that only the absolute value of the vibration amplitude can be recovered without postprocessing unwrapping methods. We have developed an advanced phase-resolved (PR) shearography method that separates the random phases from the desired signal phase. Not only is it possible to recover both amplitude and phase of the ground motion, PR shearography improves the sensitivity by up to an order of magnitude. The improved sensitivity of PR shearography can be allocated to detect smaller signals or to reduce the required seismic/acoustic excitation levels. The system also provides information needed to backpropagate surface-excitation waves and map the sources and scatterers.

The structure of this article is thus: in Sec. 2.1, the basic physics and mathematics of shearography is reviewed, followed by explanations of two-shot nonphase resolved (NPR) shearography in Sec. 2.2 and the prior state-of-the-art PS shearography in Sec. 2.3. Section 2.4 introduces our new PR shearography method, details the underlying mathematics, and summarizes its advantage relative to the previous art. In Sec. 3, the mathematical analysis of noise is provided, with an emphasis on the dominant noise source, random speckle, for the various shearography methods. In Sec. 4, confirmatory data are presented, showing the efficacy of PR shearography. Section 5 summarizes the conclusions and indicates the scope of future publications.

2 Review of Sheared Speckle Interferometry

2.1 *Shearography Optics Overview*

Each sheared specklegram represents a combination of two images that pass through separate arms of a shearing interferometer before being combined and recorded on a focal plane. A shearing interferometer operates by using a beamsplitter or other optical element to make copies of an incoming light field. An optical shearing device, such as a tilted mirror, shear plate, or other element, shifts the copies relative to each other such that a pixel representing location $\mathbf{r}$ in one copy appears at a point $(\mathbf{r} + \Delta\mathbf{r})$ in another copy. Ideally, these two light fields are identical, other than the location shift. The relatively shifted copies of the light field are optically recombined and recorded on a focal plane, creating an image called a sheared specklegram. An example of a shearing interferometer is sketched in Fig. 1.

The interferometer in Fig. 1 includes the capability to introduce known phase differences between arms of the interferometer. This enables PS shearography, as well as the PR shearography that is the subject of this paper. In Fig. 1, the phase modulation is separated from the shearing function, for simplicity of operation. However, shearing and phase modulation can be combined on the same optical element, if necessary.

Because the illumination is coherent, and the surface being illuminated is microscopically rough, the reflected light field has intensities and phases containing fluctuations that are random from point-to point so that the recorded image contains intensity fluctuations called speckles. Depending on the phase-modulating mechanisms, speckles may also be correlated with each other. The statistical fluctuations have a time dependence, which is characterized by a correlation time scale τ_C. The time τ_C is determined by the imaging conditions and can be several seconds long, though millisecond timescales are more common in terrestrial observation.

---

*Address all correspondence to Michael J. DeWeert, E-mail: michael.deweert@baesystems.com

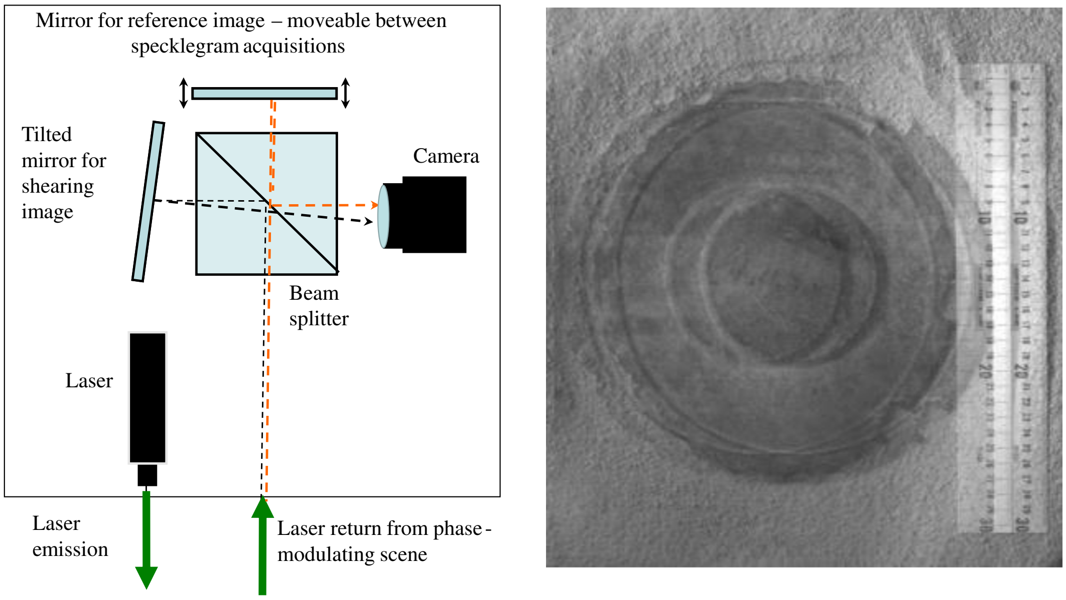

(a) Shearing interferometric imager (b) Raw sheared-specklegram example

Fig. 1 (a) Example of a shearing interferometric imager based on a Michelson-type interferometer. Many other types of shearing interferometer are possible. (b) Example of a sheared specklegram, showing superposition of images along the shear direction.

The speckle-containing optical fields are combined on a focal-plane array, which records the intensity of the combined field. Energy transport can be expressed in terms of the Poynting[1] vector:

$$\mathbf{P} = \mathbf{E}\times\mathbf{H} = \frac{1}{\mu c}\mathbf{E}\times(\hat{\mathbf{k}}\times\mathbf{E})$$
$$= \frac{1}{\mu c}[(\mathbf{E}\cdot\mathbf{E})\hat{\mathbf{k}} - (\hat{\mathbf{k}}\cdot\mathbf{E})\mathbf{E}] \approx \frac{1}{\mu c}(\mathbf{E}\cdot\mathbf{E})\hat{\mathbf{k}}. \tag{1}$$

In Eq. (1), the light propagation direction $\hat{\mathbf{k}}$ is assumed to be normal to the plane of the **E**- and **H**-fields. The integration time of the imager is also assumed to be much longer than the vibration period of the electromagnetic field so that the recorded intensity is proportional to the squared magnitude of a slowly varying complex envelope function $\mathbf{E}_S$ multiplied by the observation time T

$$\int_0^T \mathrm{d}t(\mathbf{E}\cdot\mathbf{E}) = \frac{1}{4}\int_0^T \mathrm{d}t\{\mathbf{E}_S e^{(i\mathbf{k}\cdot\mathbf{r}-\omega t)} + \mathbf{E}_S^* e^{[-(i\mathbf{k}\cdot\mathbf{r}-\omega t)]}\}$$
$$\cdot\{\mathbf{E}_S e^{(i\mathbf{k}\cdot\mathbf{r}-\omega t)} + \mathbf{E}_S^* e^{[-(i\mathbf{k}\cdot\mathbf{r}-\omega t)]}\}$$
$$= \frac{1}{2}\int_0^T \mathrm{d}t|\mathbf{E}_S|^2 + \frac{1}{4}\int_0^T \mathrm{d}t\{\mathbf{E}_S\cdot\mathbf{E}_S e^{[+2(i\mathbf{k}\cdot\mathbf{r}-\omega t)]}$$
$$+ \mathbf{E}_S^*\cdot\mathbf{E}_S^* e^{[-2(i\mathbf{k}\cdot\mathbf{r}-\omega t)]}\} = \frac{1}{2}|\mathbf{E}_S|^2 T. \tag{2}$$

The optical field $\mathbf{E}_S$ in Eq. (2) retains vector (Jones[1]) notation, due to polarization. The polarization of the optical field may vary randomly from point to point, for example, if the laser beam illuminates a birefringent material. In such cases, polarizers in the receiver aperture can significantly degrade the performance of shearography sensors. We will explore polarized-light PR shearography in a future paper. For now, we consider the case in which all polarizations are accepted equally so that the received light is approximately a complex scalar field:

$$\mathbf{E}_S = E_S(\mathbf{r}, t)\exp[i\phi(\mathbf{r}, t)], \tag{3}$$

where the time t is a smoothed average over many waves of light. In this paper, we assume that the correlation time of the light field is longer than the observation time so that

$$(\lambda/c) \ll t_{\text{Observation}} \ll \tau_C. \tag{4}$$

The time $t_{\text{Observation}}$ in Eq. (4) is any time much longer than the period λ/c of a light wave that is characteristic of a light-sensitive device. It can be, for example, the exposure time of a camera or the time constant of a photocell.

Note that the time averaging in Eq. (2) also separates different wavelengths of light so that each wavelength in a finite-temporal-width pulse may be considered independently.

For coherent light reflected from an optically rough surface, the optical field at any given locus on the focal plane (of a camera viewing the surface) represents a summation of many complex scalars with a statistical distribution of phases. This summation is entailed by the finite-sized optical spread function (OSF). Diffraction from the receiver aperture determines the minimum OSF spread. Atmospheric scattering adds additional broadening. The summing of random phasors yields a net field, which we express as

$$E_S(\mathbf{r}, t) = \int_{\text{Object}} \mathrm{d}\mathbf{r}_O \mathrm{OSF}(\mathbf{r}, \mathbf{r}_O) E_O(\mathbf{r}_O, t)\exp[i\phi_O(\mathbf{r}_O, t)], \tag{5}$$

where OSF is the complex OSF connecting the observation point $\mathbf{r}$ with an object point $\mathbf{r}_\mathrm{O}$, and E_O and ϕ_O are the reflected E-field magnitude and phase at $\mathbf{r}_\mathrm{O}$. The basic statistics are illustrated by considering the simplest case, in which the laser illumination and surface reflectance vary little as $\mathbf{r}_\mathrm{O}$ varies, and in which the phases are independent and identically distributed from point to point. The intensity at a point on the focal plane is given as

$$\begin{aligned} I(\mathbf{r},t) &= |E_S(\mathbf{r},t)|^2 \\ &\approx |E_O(\mathbf{r}_O,t)|^2 \int_{\text{Object}} \mathrm{d}\mathbf{r}_O \int_{\text{Object}} \mathrm{d}\mathbf{r}_O{}' \mathrm{OSF}(\mathbf{r},\mathbf{r}_O)\mathrm{OSF} \\ &\quad * (\mathbf{r},\mathbf{r}_O{}') \exp[i\phi_O(\mathbf{r}_O,t) - i\phi_O(\mathbf{r}_O{}',t)]. \end{aligned} \tag{6}$$

Carrying out the integral in Eq. (6) in this simplest case[2] yields an optical field of the form:

$$E_S(\mathbf{r},t) = |E_S(\mathbf{r},t)| \exp[i\phi(\mathbf{r},t)], \tag{7}$$

with intensity

$$I_S(\mathbf{r},t) = |E_S(\mathbf{r},t)|^2, \tag{8}$$

and with probability distributions

$$\begin{aligned} P(|E_S(\mathbf{r},t)|) &= 2(|E_S|/\langle I_S\rangle) \exp(-|E_S|^2/\langle I_S\rangle), \\ &\quad 0 \le |E_S| < \infty, \end{aligned} \tag{9}$$

and

$$P(\phi) = 1/(2\pi), \qquad -\pi \le \phi < +\pi. \tag{10}$$

The derivation of Eq. (9) from Eq. (6) relies on the central limit theorem, implicitly assuming that the extent of the OSF is much larger than the range of phase correlations on the object surface. The optical field probability distribution function (PDF) in Eq. (9) is an example of a Rayleigh distribution, and the intensity follows an exponential distribution:

$$P(I_S) = (1/\langle I_S\rangle) \exp(-I_S/\langle I_S\rangle), \qquad 0 \le I_S < \infty. \tag{11}$$

The significance of Eq. (11) is twofold: (a) the most-likely value of speckle intensity is zero and (b) the maximum value of intensity is infinite. Because neither dark speckles (with values below the camera noise levels) nor saturated speckles carry useable phase information, the dynamic range of the camera must be sufficient to record as many bright speckles as possible without saturation.

In a physically realizable camera, the intensities of finite-sized pixels will deviate from the exponential distribution, due to the integration of intensities over a pixel area. In the extreme case of very large pixels, the central limit theorem again dictates that the distribution of intensities tends toward a Gaussian. In practice, the intensity distribution more resembles a Gamma or log-normal distribution, with an asymmetric peak above the minimum value of zero. The more $P(I_S)$ deviates from an exponential distribution, the more diluted is the phase information, and the less usable the data are for shearography. This relationship between pixel size and speckle size constrains the camera design: in a diffraction-limited design, the optics must be slow enough (i.e., have high enough $f/\#$) that the OSF fills or over-fills each pixel.

A shearing interferometer such as that shown in Fig. 1 uses a linear shear to combine the optical fields from points $\{\mathbf{r}_\mathrm{O}\}$ with those from points $\{\mathbf{r}_\mathrm{O} + \Delta\mathbf{r}_\mathrm{Shear}\}$. It can also be operated so as to introduce an additional controlled phase difference ϕ_Step between the interferometer arms. The net time-dependent optical field at a point $\mathbf{r}$ in the combined field is

$$E_\mathrm{Total}(\mathbf{r},t) = E_S(\mathbf{r},t) + E_S(\mathbf{r}+\Delta\mathbf{r}_\mathrm{Shear},t) \exp[i\phi_\mathrm{Step}(\mathbf{r},t)]. \tag{12}$$

The time dependences in Eq. (12) apply to the slowly varying envelope, with time scales on the order of $t_\mathrm{Observation}$ described in Eq. (4). Any spatial dependence of the controlled phase step $\phi_\mathrm{Step}(\mathbf{r},t)$ is usually an unintended effect of optical aberrations, but as long as the spatial dependences are constant between observations, they have few adverse effects on shearography. Optical paths through the interferometer arms will also have uncontrolled phase differences, which typically vary over time scales longer than the correlation time τ_C and which we absorb into the random part of the optical-field phases.

From Eq. (12), the intensity of the sheared specklegram is

$$\begin{aligned} I(\mathbf{r},t) &= |E_\mathrm{Total}(\mathbf{r},t)|^2 \\ &= |E_S(\mathbf{r},t) + E_S(\mathbf{r}+\Delta\mathbf{r}_\mathrm{Shear},t)\exp[i\phi_\mathrm{Step}(\mathbf{r},t)]|^2 \\ &= \left\{ \begin{array}{l} I_S(\mathbf{r},t) + I_S(\mathbf{r}+\Delta\mathbf{r}_\mathrm{Shear},t) \\ +2\sqrt{I_S(\mathbf{r},t)I_S(\mathbf{r}+\Delta\mathbf{r}_\mathrm{Shear},t)}\cos[\phi(\mathbf{r}+\Delta\mathbf{r}_\mathrm{Shear},t) \\ -\phi(\mathbf{r},t) + \phi_\mathrm{Step}(\mathbf{r},t)] \end{array} \right\}. \end{aligned} \tag{13}$$

For direct numerical simulations and detailed statistical analysis, we use Eq. (12) or Eq. (13) directly, with surface-roughness correlations, and medium-propagation effects added as appropriate. In future papers, we will present comparisons of direct simulations to experimental data. For now, we are concerned with basic phenomenology of PR versus standard shearography methods. To simplify notation for the explanations, we follow the standard treatment,[2] rewriting Eq. (13) as

$$\begin{aligned} I(\mathbf{r},t) &= I_0(\mathbf{r},\Delta\mathbf{r}_\mathrm{Shear},t)\{1+\gamma(\mathbf{r},\Delta\mathbf{r}_\mathrm{Shear},t) \\ &\quad \times \cos[\Delta\phi(\mathbf{r},\Delta\mathbf{r}_\mathrm{Shear},t) + \phi_\mathrm{Step}(\mathbf{r},t)]\}, \end{aligned} \tag{14}$$

where

$$I_0(\mathbf{r},\Delta\mathbf{r}_\mathrm{Shear},t) = I_S(\mathbf{r},t) + I_S(\mathbf{r}+\Delta\mathbf{r}_\mathrm{Shear},t), \tag{15}$$

$$\boldsymbol{\gamma}(\mathbf{r},\Delta\mathbf{r}_\mathrm{Shear},t) = 2\sqrt{I_S(\mathbf{r},t)I_S(\mathbf{r}+\Delta\mathbf{r}_\mathrm{Shear},t)}/I_0(\mathbf{r},\Delta\mathbf{r}_\mathrm{Shear},t), \tag{16}$$

and

$$\Delta\phi(\mathbf{r},\Delta\mathbf{r}_\mathrm{Shear},t) = [\phi(\mathbf{r}+\Delta\mathbf{r}_\mathrm{Shear},t) - \phi(\mathbf{r},t)]. \tag{17}$$

The sheared phase difference $\Delta\phi(\mathbf{r},\Delta\mathbf{r}_{\text{Shear}},t)$ is composed of a random speckle component $\phi_{\text{Speckle}}(\mathbf{r},\Delta\mathbf{r}_{\text{Shear}},t)$ and a signal $\phi_{\text{Signal}}(\mathbf{r},\Delta\mathbf{r}_{\text{Shear}},t)$, so

$$\Delta\phi(\mathbf{r},\Delta\mathbf{r}_{\text{Shear}},t) = [\phi_{\text{Speckle}}(\mathbf{r},\Delta\mathbf{r}_{\text{Shear}}) + \phi_{\text{Signal}}(\mathbf{r},\Delta\mathbf{r}_{\text{Shear}},t) + \phi_{\text{Step}}(t)]. \tag{18}$$

The primary goal of shearography is to detect and quantify the signal phase ϕ_{Signal}. To accomplish this, a series of sheared specklegrams are acquired at a series of times $\{t_j\}$, with time separations that are much less than the random-speckle decorrelation time τ_C so that ϕ_{Speckle} in Eq. (18) is nearly constant with time. The image series is acquired quickly enough that the random-speckle contributions to the intensities I and contrast $\boldsymbol{\gamma}$ are constant over time. Ideally, the phase step ϕ_{Step} is designed to be uniform across each specklegram, so we can ignore its spatial dependence. With these considerations included, Eq. (14) for a sheared specklegram becomes:

$$I(\mathbf{r},t_j) = I_0(\mathbf{r},\Delta\mathbf{r}_{\text{Shear}}) \times \left\{ 1+\gamma(\mathbf{r},\Delta\mathbf{r}_{\text{Shear}})\cos\left[\begin{array}{l} \boldsymbol{\phi}_{\text{Speckle}}(\mathbf{r},\Delta\mathbf{r}_{\text{Shear}}) \\ +\boldsymbol{\phi}_{\text{Signal}}(\mathbf{r},\Delta\mathbf{r}_{\text{Shear}},t_j) \\ +\boldsymbol{\phi}_{\text{Step}}(t_j) \end{array}\right] \right\}. \tag{19}$$

The quantity $\phi_{\text{Signal}}(\mathbf{r},\Delta\mathbf{r}_{\text{Shear}},t_j)$ is the phase difference due to optical-path differences between points located at $\mathbf{r}$ and $((\mathbf{r}+\Delta\mathbf{r}_{\text{Shear}}))$. The values of $\boldsymbol{\phi}_{\text{Signal}}(\mathbf{r},\Delta\mathbf{r}_{\text{Shear}},t_j)$ can vary significantly with time in the presence of deterministic effects, such as surface vibrations, refractive-index changes, thermally induced deformations, and other physically or chemically induced changes over time. The effects causing optical phase differences are commonly referred to as loads, and their absence is commonly referred to as an unloaded condition. In the PR method, the loading can be dynamic, eliminating the need to identify unloaded or constant-load conditions.

The variability in optical phase difference $\varphi_{\text{Signal}}(\mathbf{r},\Delta\mathbf{r}_{\text{Shear}},t)$ is the quantity of interest—what the shearography system and analysis methods are designed to estimate. For the specific case of a vibrating, opaque, diffusely reflective surface, the optical phase difference is given in radians as

$$\varphi_{\text{Signal}}(\mathbf{r},\Delta\mathbf{r}_{\text{Shear}},t) = 2\times\frac{2\pi}{\lambda}\times[h(\mathbf{r}+\Delta\mathbf{r}_{\text{Shear}},t)-h(\mathbf{r},t)], \tag{20}$$

where $h(\mathbf{r},t)$ is the time-varying surface elevation at a point $\mathbf{r}$ and time t, and λ is the wavelength of the laser light. The difference in elevation between points separated by the shear distance is called the shear height. Because the wavelength of light is short, typically on the order of a micron or less, extremely small changes in shear height can be imaged.

2.2 *Basic Two-Shot Shearography*

In order to ground the discussion of PR shearography, a review of basic two-laser-shot shearography is in order. (Some terms to describe shearography are defined in Table 1.) The separate camera shots can be acquired with a camera triggered by a pulsed laser or can be frames acquired under continuous-wave illumination.

Table 1 Shearography nomenclature.

Specklegram	The image obtained by interfering two speckled wavefronts (images) in an imaging interferometer. In shearography, the interferometer is configured as a shearing interferometer. Multiple specklegrams are acquired and processed to yield a shearogram.
Shearing:	Displacing or rotating an image in its own plane, for example, by a linear displacement vector $\Delta\mathbf{r}_{\text{Shear}}$. In shearography, the sheared image is the complex optical field before detection on a focal plane.
Shearogram	The image produced by processing multiple specklegrams created with a shearing interferometer. Fringe boundaries are visible where there is high correlation between the random components of the specklegrams. This occurs whenever the optical phase difference between the specklegrams (at a given pixel) equals zero or an integral number of wavelengths of optical path difference.
Shearogram fringes:	Generic term for patterns of fringes that appear in shearograms as a consequence of surface change. In the special case of a surface containing circularly symmetric time-varying bumps, typical shearogram fringes appear as "butterfly" shapes. (Examples of butterfly shearograms are shown in Sec. 4)
Shear height	The maximum change in the difference in elevation between points separated by the shear vector $\Delta\mathbf{r}_{\text{Shear}}$, during the interval between the first and last image used to produce a shearogram.

The simplest shearogram-generation method uses two specklegrams, with the load changed in the time between their acquisitions, and $\boldsymbol{\phi}_{\text{Step}}$ kept equal to zero. Define the specklegram image acquired at time t_j by $\mathbf{S}_j=\mathbf{I}(j)$. Then, using Eq. (19), the difference of specklegrams acquired at t_1 and t_2 is a shearogram given as

$$\begin{aligned}[\mathbf{S}_2-\mathbf{S}_1] &= \mathbf{I}_0.*\boldsymbol{\gamma}.*\{\cos[\boldsymbol{\phi}_{\text{Speckle}}+\boldsymbol{\phi}_{\text{Signal}}(2)] \\ &\quad -\cos[\boldsymbol{\phi}_{\text{Speckle}}+\boldsymbol{\phi}_{\text{Signal}}(1)]\} \\ &= \mathbf{I}_0.*\boldsymbol{\gamma}.*\left\{\begin{array}{l}(\cos\boldsymbol{\phi}_{\text{Speckle}}).*[\cos\boldsymbol{\phi}_{\text{Signal}}(2)-\cos\boldsymbol{\phi}_{\text{Signal}}(1)] \\ -(\sin\boldsymbol{\phi}_{\text{Speckle}}).*[\sin\boldsymbol{\phi}_{\text{Signal}}(2)-\sin\boldsymbol{\phi}_{\text{Signal}}(1)]\end{array}\right\}.\end{aligned} \tag{21}$$

Equation (21) is cast in a notation that treats the images as time-dependent matrices, with the spatial coordinates $\mathbf{r}$ replaced by matrix indices. The operator ".*" indicates an element-by element multiplication of matrix elements (i.e., a Hadamard or Schur product), and the trigonometric functions operate element-by-element on their arguments. In the case of small signal phases ($\ll 1$ wave of light), Eq. (21) reduces to

$$\begin{aligned}[\mathbf{S}(2)-\mathbf{S}(1)] &\approx (-\mathbf{I}_0.*\boldsymbol{\gamma}.*\sin\boldsymbol{\phi}_{\text{Speckle}}). \\ &\quad *[\boldsymbol{\phi}_{\text{Signal}}(2)-\boldsymbol{\phi}_{\text{Signal}}(1)].\end{aligned} \tag{22}$$

The structure of Eq. (22) shows that the shearogram is an image of random noise $(-\mathbf{I}_0.*\boldsymbol{\gamma}.*\sin\boldsymbol{\phi}_{\text{Speckle}})$, modulated by an image of signal phase changes $[\boldsymbol{\phi}_{\text{Signal}}(2)-\boldsymbol{\phi}_{\text{Signal}}(1)]$. Because the phases of the speckle noise $\boldsymbol{\phi}_{\text{Speckle}}$ are random, only the magnitude of the signal phase is available—the signal sign is ambiguous. Furthermore, the random noise is typically so high that it is difficult to detect small-amplitude phases through the noisy background in two-shot shearography. A noise analysis is presented in Sec. 3.

2.3 *Prior Art: Phase-Stepped Shearogram Analysis*

The goal of specklegram-image analysis is to estimate the signal $\boldsymbol{\phi}_{\text{Signal}}(t)$ with as little error as possible, despite the speckle noise in $\mathbf{I_0}$, $\boldsymbol{\gamma}$, and $\boldsymbol{\phi}_{\text{Speckle}}$. Inspection of Eq. (22) shows that the noisy terms $\mathbf{I_0}$ and $\boldsymbol{\gamma}$ can be removed by computing ratios of differences of specklegrams. All that is required is that all of the specklegrams are acquired within a time span shorter than the correlation time τ_C. For example, with $\boldsymbol{\phi}_{\text{Step}}(i) = (3\pi/2)$, $\boldsymbol{\phi}_{\text{Step}}(j) = (\pi/2)$, $\boldsymbol{\phi}_{\text{Step}}(k) = 0$, and $\boldsymbol{\phi}_{\text{Step}}(l) = \pi$, we obtain

$$\mathbf{R_{i,j;k,l}} = \frac{[\mathbf{S}_i - \mathbf{S}_j]}{[\mathbf{S}_k - \mathbf{S}_l]} \approx \frac{\sqrt{\mathbf{I}_0 \mathbf{I}_{\Delta\mathbf{r}}}\{\cos[\boldsymbol{\phi}_{\text{Speckle}} + \boldsymbol{\phi}_{\text{Signal}}(A) + 3\pi/2] - \cos[\boldsymbol{\phi}_{\text{Speckle}} + \boldsymbol{\phi}_{\text{Signal}}(A) + \pi/2]\}}{\sqrt{\mathbf{I}_0 \mathbf{I}_{\Delta\mathbf{r}}}\{\cos[\boldsymbol{\phi}_{\text{Speckle}} + \boldsymbol{\phi}_{\text{Signal}}(A)] - \cos[\boldsymbol{\phi}_{\text{Speckle}} + \boldsymbol{\phi}_{\text{Signal}}(A) + \pi]\}}. \tag{23}$$

The ratios of cosines in Eq. (23) can vary randomly between ±∞ and provide little information about the signal phases. Standard PS shearography[3] addresses this by introducing specific shot-dependent values for the controlled phases $\boldsymbol{\phi}_{\text{Step}}(j)$ and synchronizes the specklegram collection with the loading conditions. For each shot j, $\boldsymbol{\phi}_{\text{Step}}(j)$ is constant across the image. For a given loading condition Load_A, multiple specklegrams are collected with different $\boldsymbol{\phi}_{\text{Step}}$ values. The specklegrams can be sequential or spatially multiplexed,[4] as long as the load is constant during their acquisition. With the load held constant for a set of specklegrams, Eq. (23) becomes

$$\mathbf{R_{Load\_A}} \approx \frac{\cos[\boldsymbol{\phi}_{\text{Speckle}} + \boldsymbol{\phi}_{\text{Signal}}(A) + \boldsymbol{\phi}_{\text{Step}}(i)] - \cos[\boldsymbol{\phi}_{\text{Speckle}} + \boldsymbol{\phi}_{\text{Signal}}(A) + \boldsymbol{\phi}_{\text{Step}}(j)]}{\cos[\boldsymbol{\phi}_{\text{Speckle}} + \boldsymbol{\phi}_{\text{Signal}}(A) + \boldsymbol{\phi}_{\text{Step}}(k)] - \cos[\boldsymbol{\phi}_{\text{Speckle}} + \boldsymbol{\phi}_{\text{Signal}}(A) + \boldsymbol{\phi}_{\text{Step}}(l)]}, \tag{24}$$

which after expanding the trigonometric functions reduces to

$$\mathbf{R}_{\text{Load\_A}} \approx \frac{[\cos\,\boldsymbol{\phi}_{\text{Step}}(i) - \cos\,\boldsymbol{\phi}_{\text{Step}}(j)] - \tan[\boldsymbol{\phi}_{\text{Signal}}(A) + \boldsymbol{\phi}_{\text{Speckle}}].*[\sin\,\boldsymbol{\phi}_{\text{Step}}(i) - \sin\,\boldsymbol{\phi}_{\text{Step}}(j)]}{[\cos\,\boldsymbol{\phi}_{\text{Step}}(k) - \cos\,\boldsymbol{\phi}_{\text{Step}}(l)] - \tan[\boldsymbol{\phi}_{\text{Signal}}(A) + \boldsymbol{\phi}_{\text{Speckle}}].*[\sin\,\boldsymbol{\phi}_{\text{Step}}(k) - \sin\,\boldsymbol{\phi}_{\text{Step}}(l)]}, \tag{25}$$

where the ratio is also an element-by-element (Hadamard) operation.

Equation (25) is formally invertible to yield the sum of signal and noise phases

$$\arctan\left\{\frac{\mathbf{R_{Load\_A}}.*[\cos\,\boldsymbol{\phi}_{\text{Step}}(k) - \cos\,\boldsymbol{\phi}_{\text{Step}}(l)] - [\cos\,\boldsymbol{\phi}_{\text{Step}}(i) - \cos\,\boldsymbol{\phi}_{\text{Step}}(j)]}{\mathbf{R_{Load\_A}}.*[\sin\,\boldsymbol{\phi}_{\text{Step}}(k) - \sin\,\boldsymbol{\phi}_{\text{Step}}(l)] - [\sin\,\boldsymbol{\phi}_{\text{Step}}(i) - \sin\,\boldsymbol{\phi}_{\text{Step}}(j)]}\right\} = \arctan\{\tan[\boldsymbol{\phi}_{\text{Signal}}(A) + \boldsymbol{\phi}_{\text{Speckle}}]\}. \tag{26}$$

A common choice of the controlled phases is

$$\boldsymbol{\phi}_{\text{Step}}(i) = (3\pi/2), \quad \boldsymbol{\phi}_{\text{Step}}(j) = (\pi/2),$$
$$\boldsymbol{\phi}_{\text{Step}}(k) = 0, \quad \text{and} \quad \boldsymbol{\phi}_{\text{Step}}(l) = \pi, \tag{27}$$

in which case Eq. (25) reduces to

$$\arctan(\mathbf{R_{Load\_A}}) \approx \arctan\{\tan[\boldsymbol{\phi}_{\text{Signal}}(A) + \boldsymbol{\phi}_{\text{Speckle}}]\}. \tag{28}$$

Using four-quadrant inversions to compute the inverse tangent, Eq. (28) actually yields, in terms of the noise and signal phases

$$\arctan\{\tan[\boldsymbol{\phi}_{\text{Signal}}(A) + \boldsymbol{\phi}_{\text{Speckle}}]\} \approx [\boldsymbol{\phi}_{\text{Signal}}(A) + \boldsymbol{\phi}_{\text{Speckle}}] + \mathbf{N}[\boldsymbol{\phi}_{\text{Speckle}}, \boldsymbol{\phi}_{\text{Signal}}(A)], \tag{29}$$

where

$$\mathbf{N}[\boldsymbol{\phi}_{\text{Speckle}}, \boldsymbol{\phi}_{\text{Signal}}(A)] = \begin{cases} -2\pi\Theta\{\boldsymbol{\phi}_{\text{Speckle}} - [\pi - \boldsymbol{\phi}_{\text{Signal}}(A)]\}, & \pi > \boldsymbol{\phi}_{\text{Signal}}(A) \geq 0 \\ +2\pi\Theta\{\boldsymbol{\phi}_{\text{Speckle}} - [-\pi - \boldsymbol{\phi}_{\text{Signal}}(A)]\}, & -\pi \leq \boldsymbol{\phi}_{\text{Signal}}(A) < 0 \end{cases}. \tag{30}$$

In Eq. (29), both $\boldsymbol{\phi}_{\text{Signal}}$ and $\boldsymbol{\phi}_{\text{Speckle}}$ are defined modulus 2π on the interval $(-\pi, +\pi)$, and the unit step function Θ is

$$\Theta(x) = \begin{cases} 0, & x < 0 \\ 1, & x \geq 0 \end{cases}. \tag{31}$$

Because the random phases $\boldsymbol{\phi}_{\text{Speckle}}$ span the full 2π radian range of possible phases, Eq. (29) does not yield a usable image of the signal phases. To obtain a usable estimate, another loading condition Load_B must be applied, and the PS image acquisition repeated. If the second set of images is acquired within the correlation time τ_C, then the signal phase differences can be computed from two successive ratio calculations, to yield a PS shearogram:

$$\{\arctan[\tan \boldsymbol{\phi}_{\mathrm{Signal}}(B)] - \arctan[\tan \boldsymbol{\phi}_{\mathrm{Signal}}(A)]\} \\ \approx [\arctan(\mathbf{R}_{\mathbf{Load\_B}}) - \arctan(\mathbf{R}_{\mathbf{Load\_A}})]. \tag{32}$$

With Eq. (29) inserted, Eq. (32) yields

$$X_{\mathrm{PS}} = X_0 + \{\mathbf{N}[\boldsymbol{\phi}_{\mathrm{Speckle}}, \boldsymbol{\phi}_{\mathrm{Signal}}(B)] - \mathbf{N}[\boldsymbol{\phi}_{\mathrm{Speckle}}, \boldsymbol{\phi}_{\mathrm{Signal}}(A)]\}, \tag{33}$$

where

$$X_{\mathrm{PS}} = [\arctan(\mathbf{R}_{\mathbf{Load\_B}}) - \arctan(\mathbf{R}_{\mathbf{Load\_A}})], \tag{34}$$

is the signal-change estimate, and

$$X_0 = [\boldsymbol{\phi}_{\mathrm{Signal}}(B) - \boldsymbol{\phi}_{\mathrm{Signal}}(A)], \tag{35}$$

is the ideal noise-free result.

Due to the wrap-around properties of trigonometric functions and inversions, Eq. (33) gives an image of the load-induced signal-phase variation but with speckle noise.

In much of the PS shearography literature, noise terms are completely ignored and $X_{\mathrm{PS}} = X_0$ is directly presented at the final result. The speckle-noise terms in Eq. (33) are

$$\left\{\mathbf{N}[\boldsymbol{\phi}_{\mathrm{Speckle}}, \boldsymbol{\phi}_{\mathrm{Signal}}(B)] - \mathbf{N}[\boldsymbol{\phi}_{\mathrm{Speckle}}, \boldsymbol{\phi}_{\mathrm{Signal}}(A)]\right\} \\ = \begin{cases} 2\pi \begin{Bmatrix} -\Theta[\boldsymbol{\phi}_{\mathrm{Speckle}} + \boldsymbol{\phi}_{\mathrm{Signal}}(B) - \pi] \\ +\Theta[\boldsymbol{\phi}_{\mathrm{Speckle}} + \boldsymbol{\phi}_{\mathrm{Signal}}(A) - \pi] \end{Bmatrix}, & \boldsymbol{\phi}_{\mathrm{Signal}}(A) \geq 0 \text{ and } \boldsymbol{\phi}_{\mathrm{Signal}}(B) \geq 0 \\ -2\pi \begin{Bmatrix} \Theta[\boldsymbol{\phi}_{\mathrm{Speckle}} + \boldsymbol{\phi}_{\mathrm{Signal}}(B) - \pi] \\ +\Theta[\boldsymbol{\phi}_{\mathrm{Speckle}} + \boldsymbol{\phi}_{\mathrm{Signal}}(A) + \pi] \end{Bmatrix}, & \boldsymbol{\phi}_{\mathrm{Signal}}(A) < 0 \text{ and } \boldsymbol{\phi}_{\mathrm{Signal}}(B) \geq 0 \\ +2\pi \begin{Bmatrix} \Theta[\boldsymbol{\phi}_{\mathrm{Speckle}} + \boldsymbol{\phi}_{\mathrm{Signal}}(B) + \pi] \\ +\Theta[\boldsymbol{\phi}_{\mathrm{Speckle}} + \boldsymbol{\phi}_{\mathrm{Signal}}(A) - \pi] \end{Bmatrix}, & \boldsymbol{\phi}_{\mathrm{Signal}}(A) \geq 0 \text{ and } \boldsymbol{\phi}_{\mathrm{Signal}}(B) < 0 \\ +2\pi \begin{Bmatrix} \Theta[\boldsymbol{\phi}_{\mathrm{Speckle}} + \boldsymbol{\phi}_{\mathrm{Signal}}(B) + \pi] \\ -\Theta[\boldsymbol{\phi}_{\mathrm{Speckle}} + \boldsymbol{\phi}_{\mathrm{Signal}}(A) + \pi] \end{Bmatrix}, & \boldsymbol{\phi}_{\mathrm{Signal}}(A) < 0 \text{ and } \boldsymbol{\phi}_{\mathrm{Signal}}(B) < 0 \end{cases} \tag{36}$$

Equation (36) implies that the speckle noise vanishes as the signal change vanishes, providing vastly improved performance versus two-shot nonphase-stepped shearography. The nonspeckle sources do not vanish and some can reintroduce the speckle noise at any signal level. A fuller treatment of noise, for PR shearography, will be the subject of a future paper.

Equation (33) can also be obtained using two sets of three (instead of four) specklegrams, if the phase steps are chosen to be

$$\boldsymbol{\phi}_{\mathrm{Step}}(1) = 0, \quad \boldsymbol{\phi}_{\mathrm{Step}}(2) = (2\pi/3), \quad \text{and} \quad \boldsymbol{\phi}_{\mathrm{Step}}(3) \\ = (4\pi/3). \tag{37}$$

In which case, the ratios to be used in Eq. (32) are

$$\mathbf{R}_{\mathbf{Load\_A\,or\,B}} = \sqrt{3}\left.\frac{[\mathbf{S}(2) - \mathbf{S}(3)]}{[\mathbf{S}(1) - \mathbf{S}(2)] + [\mathbf{S}(1) - \mathbf{S}(3)]}\right|_{\mathbf{Load\_A\,or\,B}}. \tag{38}$$

Thus, the previous state-of-the-art requires at least six specklegrams in order to yield the signal phase changes between loading conditions. In the most-basic implementation, the specklegrams must be acquired in groups for which the loading conditions are constant. This is readily accomplished for quasistatic loads under the control of the investigator: load A is applied, the system is allowed to settle, PS specklegrams (at least 3) are acquired, then load B is applied, the system is again allowed to settle, and another set of PS specklegrams is acquired.

If the signal varies with time too quickly for quasistatic operation, then the load must be controlled or predicted in such a way that the controlled phases are synchronized with the signal phase so that sets of specklegrams having the same relationships of phase steps to signal phases can be acquired. For example, if the surface loading varies periodically with a period T, then acquiring specklegrams with phases $\boldsymbol{\phi}_{\mathrm{Step}}(1)$, $\boldsymbol{\phi}_{\mathrm{Step}}(2)$, and $\boldsymbol{\phi}_{\mathrm{Step}}(3)$ at times T_A, $T_A + T$, and $T_A + 2T$, respectively, would yield specklegrams for load A. Similarly, acquiring specklegrams with phases $\boldsymbol{\phi}_{\mathrm{Step}}(1)$, $\boldsymbol{\phi}_{\mathrm{Step}}(2)$, and $\boldsymbol{\phi}_{\mathrm{Step}}(3)$, at times T_B, $T_B + T$, and $T_B + 2T$, respectively, would yield specklegrams for load B. The system operator chooses the difference between T_A and T_B to maximize the likelihood of a significant signal difference.

The set of requirements that: (1) the controlled phases in the shearography system be synchronized with the loading conditions and (2) that at least two groups of specklegrams be used to construct a shearogram is a significant limiter of performance for very dynamic conditions in which the investigator cannot control or predict the loading of the area being investigated, or in which the time to acquire synchronized sets of specklegrams exceeds τ_C. Examples include imaging in situations in which dwell times are limited by hazardous conditions (as in a combat situation), or in which the excitation causing the loading is transient and not controlled by the investigator. One alternative is to construct shearograms by differencing specklegrams acquired under loading conditions with constant phase steps (that is, with no phase stepping at all), implementing Eq. (22). This two-shot approach yields very noisy estimates of the differences between loading conditions, typically requiring many repeated measurements to achieve high sensitivity, limiting the performance of the measurement system for dynamic phenomena.

An alternative to sequential phase-stepping is to implement a spatial-multiplexing method, such as in Ref. 4, then apply Eq. (32). Spatial multiplexing sacrifices spatial resolution in order to achieve faster PS image acquisition.

An additional cost of spatial multiplexing is that the imaging system must operate at a higher $f/\#$, because the camera blur function must distribute phase information over a multipixel area that is typically four times the area of a single pixel. A higher $f/\#$ requires increasing the laser power to compensate for the reduced light-gathering power of the optics. Trading resolution and sensitivity for speed is not always possible or desirable, so we have developed another approach: PR shearography.

2.4 *Phase-Resolved Shearography Separates Signal and Speckle Phase Dynamically*

In PR shearography, achieving a highly sensitive estimate of the signal phase:

- requires four (not six or eight) images,
- computes a single shearogram,
- exploits uncontrolled (asynchronous) loading conditions,
- operates at the full resolution of the optics, and
- provides unambiguous signal-phase-gradient signs.

The mathematical underpinnings are based on Eq. (19), with the trigonometric functions expanded as follows:

$$\begin{aligned}\cos[&\boldsymbol{\phi}_{\text{Speckle}} + \boldsymbol{\phi}_{\text{Signal}}(i) + \boldsymbol{\phi}_{\text{Step}}(i)]\\ &= \cos[\boldsymbol{\phi}_{\text{Signal}}(i) + \boldsymbol{\phi}_{\text{Step}}(i)] .* \cos \boldsymbol{\phi}_{\text{Speckle}}\\ &\quad + \sin[\boldsymbol{\phi}_{\text{Signal}}(i) + \boldsymbol{\phi}_{\text{Step}}(i)] .* \sin \boldsymbol{\phi}_{\text{Speckle}}. \end{aligned} \tag{39}$$

The controlled phase $\boldsymbol{\phi}_{\text{Step}}(i)$ is varied for every image as the load changes over time. Substituting Eq. (39) into Eq. (23) gives

$$\begin{aligned}\mathbf{R}_{i,j;k,l} &= [\mathbf{S}_i - \mathbf{S}_j]/[\mathbf{S}_k - \mathbf{S}_l]\\ &\approx \frac{\cos[\boldsymbol{\phi}_{\text{Speckle}} + \boldsymbol{\phi}_{\text{Signal}}(i) + \boldsymbol{\phi}_{\text{Step}}(i)] - \cos[\boldsymbol{\phi}_{\text{Speckle}} + \boldsymbol{\phi}_{\text{Signal}}(j) + \boldsymbol{\phi}_{\text{Step}}(j)]}{\cos[\boldsymbol{\phi}_{\text{Speckle}} + \boldsymbol{\phi}_{\text{Signal}}(k) + \boldsymbol{\phi}_{\text{Step}}(k)] - \cos[\boldsymbol{\phi}_{\text{Speckle}} + \boldsymbol{\phi}_{\text{Signal}}(l) + \boldsymbol{\phi}_{\text{Step}}(l)]}\\ &\approx \frac{\left\{\begin{matrix}\cos[\boldsymbol{\phi}_{\text{Signal}}(i) + \boldsymbol{\phi}_{\text{Step}}(i)]\\ -\cos[\boldsymbol{\phi}_{\text{Signal}}(j) + \boldsymbol{\phi}_{\text{Step}}(j)]\end{matrix}\right\} .* \cot \boldsymbol{\phi}_{\text{Speckle}} - \left\{\begin{matrix}\sin[\boldsymbol{\phi}_{\text{Signal}}(i) + \boldsymbol{\phi}_{\text{Step}}(i)]\\ -\sin[\boldsymbol{\phi}_{\text{Signal}}(j) + \boldsymbol{\phi}_{\text{Step}}(j)]\end{matrix}\right\}}{\left\{\begin{matrix}\cos[\boldsymbol{\phi}_{\text{Signal}}(k) + \boldsymbol{\phi}_{\text{Step}}(k)]\\ -\cos[\boldsymbol{\phi}_{\text{Signal}}(l) + \boldsymbol{\phi}_{\text{Step}}(l)]\end{matrix}\right\} .* \cot \boldsymbol{\phi}_{\text{Speckle}} - \left\{\begin{matrix}\sin[\boldsymbol{\phi}_{\text{Signal}}(k) + \boldsymbol{\phi}_{\text{Step}}(k)]\\ -\sin[\boldsymbol{\phi}_{\text{Signal}}(l) + \boldsymbol{\phi}_{\text{Step}}(l)]\end{matrix}\right\}},\end{aligned} \tag{40}$$

where

$$\cot \boldsymbol{\phi}_{\text{Speckle}} = \cos \boldsymbol{\phi}_{\text{Speckle}} ./ \sin \boldsymbol{\phi}_{\text{Speckle}}. \tag{41}$$

In Eq. (40), all of the random speckle noise is in the terms proportional to $(\cot \boldsymbol{\phi}_{\text{Speckle}})$, so it is possible to dynamically vary the controlled phases $\{\boldsymbol{\phi}_{\text{Step}}(j)\}$ so as to minimize the speckle noise in the shearogram $\mathbf{R}$. For the cases of very small signal phases, it is even possible to make the speckle noise terms infinitesimal, providing exquisite sensitivity to signal phases.

To see this, consider a surface moving under continuously time-varying load such that points separated by the shear distance move with a time-varying relative amplitude $\boldsymbol{\phi}(t)$, which is a small fraction of the wavelength of the laser radiation. For a four-shot series, expand the trigonometric functions in Eq. (40) to give

$$\begin{aligned}\mathbf{R}_{i,j;k,l} &= [\mathbf{S}_i - \mathbf{S}_j]/[\mathbf{S}_k - \mathbf{S}_l]\\ &\approx \frac{\cos[\boldsymbol{\phi}_{\text{Speckle}} + \boldsymbol{\phi}_{\text{Signal}}(i) + \boldsymbol{\phi}_{\text{Step}}(i)] - \cos[\boldsymbol{\phi}_{\text{Speckle}} + \boldsymbol{\phi}_{\text{Signal}}(j) + \boldsymbol{\phi}_{\text{Step}}(j)]}{\cos[\boldsymbol{\phi}_{\text{Speckle}} + \boldsymbol{\phi}_{\text{Signal}}(k) + \boldsymbol{\phi}_{\text{Step}}(k)] - \cos[\boldsymbol{\phi}_{\text{Speckle}} + \boldsymbol{\phi}_{\text{Signal}}(l) + \boldsymbol{\phi}_{\text{Step}}(l)]}\\ &= \frac{\left\{\begin{matrix}\cos[\boldsymbol{\phi}_{\text{Signal}}(i) + \boldsymbol{\phi}_{\text{Step}}(i)]\\ -\cos[\boldsymbol{\phi}_{\text{Signal}}(j) + \boldsymbol{\phi}_{\text{Step}}(j)]\end{matrix}\right\} .* \cot \boldsymbol{\phi}_{\text{Speckle}} - \left\{\begin{matrix}\sin[\boldsymbol{\phi}_{\text{Signal}}(i) + \boldsymbol{\phi}_{\text{Step}}(i)]\\ -\sin[\boldsymbol{\phi}_{\text{Signal}}(j) + \boldsymbol{\phi}_{\text{Step}}(j)]\end{matrix}\right\}}{\left\{\begin{matrix}\cos[\boldsymbol{\phi}_{\text{Signal}}(k) + \boldsymbol{\phi}_{\text{Step}}(k)]\\ -\cos[\boldsymbol{\phi}_{\text{Signal}}(l) + \boldsymbol{\phi}_{\text{Step}}(l)]\end{matrix}\right\} .* \cot \boldsymbol{\phi}_{\text{Speckle}} - \left\{\begin{matrix}\sin[\boldsymbol{\phi}_{\text{Signal}}(k) + \boldsymbol{\phi}_{\text{Step}}(k)]\\ -\sin[\boldsymbol{\phi}_{\text{Signal}}(l) + \boldsymbol{\phi}_{\text{Step}}(l)]\end{matrix}\right\}}.\end{aligned} \tag{42}$$

If the phase-steps are chosen so that

$$\begin{aligned}&\cos \boldsymbol{\phi}_{\text{Step}}(4) = \cos \boldsymbol{\phi}_{\text{Step}}(1) = 1,\\ &\sin \boldsymbol{\phi}_{\text{Step}}(4) = \sin \boldsymbol{\phi}_{\text{Step}}(1) = 0,\\ &\cos \boldsymbol{\phi}_{\text{Step}}(3) = \cos \boldsymbol{\phi}_{\text{Step}}(2), \text{ and}\\ &\sin \boldsymbol{\phi}_{\text{Step}}(3) = -\sin \boldsymbol{\phi}_{\text{Step}}(2) \neq 0,\end{aligned} \tag{43}$$

and we use the relations

$$\begin{aligned}\cos[&\boldsymbol{\phi}_{\text{Signal}}(i) + \boldsymbol{\phi}_{\text{Step}}(i)]\\ &= [\cos \boldsymbol{\phi}_{\text{Signal}}(i) \cos \boldsymbol{\phi}_{\text{Step}}(i) - \sin \boldsymbol{\phi}_{\text{Signal}}(i) \sin \boldsymbol{\phi}_{\text{Step}}(i)],\\ &\text{and}\\ \sin[&\boldsymbol{\phi}_{\text{Signal}}(i) + \boldsymbol{\phi}_{\text{Step}}(i)]\\ &= [\cos \boldsymbol{\phi}_{\text{Signal}}(i) \sin \boldsymbol{\phi}_{\text{Step}}(i) + \sin \boldsymbol{\phi}_{\text{Signal}}(i) \cos \boldsymbol{\phi}_{\text{Step}}(i)],\\ &\text{then:}\end{aligned} \tag{44}$$

$$\begin{aligned}
\mathbf{R}_{4,1;3,2} &\approx \frac{\left\{\begin{array}{l}\cos[\phi_{\text{Signal}}(4)+\phi_{\text{Step}}(4)]\\ -\cos[\phi_{\text{Signal}}(1)+\phi_{\text{Step}}(1)]\end{array}\right\}.*\cot\phi_{\text{Speckle}}-\left\{\begin{array}{l}\sin[\phi_{\text{Signal}}(4)+\phi_{\text{Step}}(4)]\\ -\sin[\phi_{\text{Signal}}(1)+\phi_{\text{Step}}(1)]\end{array}\right\}}{\left\{\begin{array}{l}\cos[\phi_{\text{Signal}}(3)+\phi_{\text{Step}}(3)]\\ -\cos[\phi_{\text{Signal}}(2)+\phi_{\text{Step}}(2)]\end{array}\right\}.*\cot\phi_{\text{Speckle}}-\left\{\begin{array}{l}\sin[\phi_{\text{Signal}}(3)+\phi_{\text{Step}}(3)]\\ -\sin[\phi_{\text{Signal}}(2)+\phi_{\text{Step}}(2)]\end{array}\right\}}\\
&\approx \frac{\left[\begin{array}{l}\left\{\begin{array}{l}[\cos\phi_{\text{Signal}}(4)\cos\phi_{\text{Step}}(4)-\sin\phi_{\text{Signal}}(4)\sin\phi_{\text{Step}}(4)]\\ -[\cos\phi_{\text{Signal}}(1)\cos\phi_{\text{Step}}(1)-\sin\phi_{\text{Signal}}(1)\sin\phi_{\text{Step}}(1)]\end{array}\right\}.*\cot\phi_{\text{Speckle}}\\ -\left\{\begin{array}{l}[\cos\phi_{\text{Signal}}(4)\sin\phi_{\text{Step}}(4)+\sin\phi_{\text{Signal}}(4)\cos\phi_{\text{Step}}(4)]\\ -[\cos\phi_{\text{Signal}}(1)\sin\phi_{\text{Step}}(1)+\sin\phi_{\text{Signal}}(1)\cos\phi_{\text{Step}}(1)]\end{array}\right\}\end{array}\right]}{\left[\begin{array}{l}\left\{\begin{array}{l}[\cos\phi_{\text{Signal}}(3)\cos\phi_{\text{Step}}(3)-\sin\phi_{\text{Signal}}(3)\sin\phi_{\text{Step}}(3)]\\ -[\cos\phi_{\text{Signal}}(2)\cos\phi_{\text{Step}}(2)-\sin\phi_{\text{Signal}}(2)\sin\phi_{\text{Step}}(2)]\end{array}\right\}.*\cot\phi_{\text{Speckle}}\\ -\left\{\begin{array}{l}[\cos\phi_{\text{Signal}}(3)\sin\phi_{\text{Step}}(3)+\sin\phi_{\text{Signal}}(3)\cos\phi_{\text{Step}}(3)]\\ -[\cos\phi_{\text{Signal}}(2)\sin\phi_{\text{Step}}(2)+\sin\phi_{\text{Signal}}(2)\cos\phi_{\text{Step}}(2)]\end{array}\right\}\end{array}\right]}\\
&\approx \frac{\left\{\begin{array}{l}[\cos\phi_{\text{Signal}}(4)-\cos\phi_{\text{Signal}}(1)].*\cot\phi_{\text{Speckle}}\\ -[\sin\phi_{\text{Signal}}(4)-\sin\phi_{\text{Signal}}(1)]\end{array}\right\}}{\left[\begin{array}{l}\left\{\begin{array}{l}[\cos\phi_{\text{Signal}}(3)-\cos\phi_{\text{Signal}}(2)]\cos\phi_{\text{Step}}(2)\\ +[\sin\phi_{\text{Signal}}(3)+\sin\phi_{\text{Signal}}(2)]\sin\phi_{\text{Step}}(2)\end{array}\right\}.*\cot\phi_{\text{Speckle}}\\ +\left\{\begin{array}{l}[\cos\phi_{\text{Signal}}(3)+\cos\phi_{\text{Signal}}(2)]\sin\phi_{\text{Step}}(2)\\ -[\sin\phi_{\text{Signal}}(3)-\sin\phi_{\text{Signal}}(2)]\cos\phi_{\text{Step}}(2)\end{array}\right\}\end{array}\right]}
\end{aligned}\tag{45}$$

For small signals, $\cos\phi_{\text{Signal}}(j)\approx 1$ (to second order), and $\sin\phi_{\text{Signal}}(j)\ll 1$. For a system chosen to have a significant step size, $\sin\phi_{\text{Signal}}(j)\ll\sin\phi_{\text{Step}}(2)$, then, to first order in signal phase, we obtain the PR shearogram

$$\begin{aligned}
&\textbf{Shearogram}_{PR}\equiv\mathbf{R}_{4,1;3,2}\\
&\quad\approx\frac{\{[\cos\phi_{\text{Signal}}(4)-\cos\phi_{\text{Signal}}(1)].*\cot\phi_{\text{Speckle}}-[\sin\phi_{\text{Signal}}(4)-\sin\phi_{\text{Signal}}(1)]\}}{\left[\begin{array}{l}\left\{\begin{array}{l}[\cos\phi_{\text{Signal}}(3)-\cos\phi_{\text{Signal}}(2)]\cos\phi_{\text{Step}}(2)\\ +[\sin\phi_{\text{Signal}}(3)+\sin\phi_{\text{Signal}}(2)]\sin\phi_{\text{Step}}(2)\end{array}\right\}.*\cot\phi_{\text{Speckle}}\\ +\left\{\begin{array}{l}[\cos\phi_{\text{Signal}}(3)+\cos\phi_{\text{Signal}}(2)]\sin\phi_{\text{Step}}(2)\\ -[\sin\phi_{\text{Signal}}(3)-\sin\phi_{\text{Signal}}(2)]\cos\phi_{\text{Step}}(2)\end{array}\right\}\end{array}\right]}\\
&\quad\approx\frac{-[\sin\phi_{\text{Signal}}(4)-\sin\phi_{\text{Signal}}(1)]}{\left\{\begin{array}{l}+2\sin\phi_{\text{Step}}(2)+[\sin\phi_{\text{Signal}}(3)+\sin\phi_{\text{Signal}}(2)]\sin\phi_{\text{Step}}(2).*\cot\phi_{\text{Speckle}}\\ -[\sin\phi_{\text{Signal}}(3)-\sin\phi_{\text{Signal}}(2)].*\cos\phi_{\text{Step}}(2)\end{array}\right\}}\\
&\quad\approx\mathbf{K}.*[\sin\phi_{\text{Signal}}(4)-\sin\phi_{\text{Signal}}(1)].
\end{aligned}\tag{46}$$

If the phase-stepping optics are well designed, then

$$\mathbf{K}=-0.5/\sin\phi_{\text{Step}}(2),\tag{47}$$

is a scalar, constant across the image. For small signals, the first-order approximation

$$\begin{aligned}
&\left\{\begin{array}{l}2\sin\phi_{\text{Step}}(2)\\ +[\sin\phi_{\text{Signal}}(3)+\sin\phi_{\text{Signal}}(2)]\sin\phi_{\text{Step}}(2).*\cot\phi_{\text{Speckle}}\\ -[\sin\phi_{\text{Signal}}(3)-\sin\phi_{\text{Signal}}(2)].*\cos\phi_{\text{Step}}(2)\end{array}\right\}\\
&\approx 2\sin\phi_{\text{Step}}(2),
\end{aligned}\tag{48}$$

is justified by (1) the fact that the numerator of Eq. (46) is already first order in signal, and (2) the relative rarity of speckles for which the magnitude of $\cot\phi_{\text{Speckle}}$ is significant compared to $1/\sin\phi_{\text{Signal}}(j)$.

The significance of Eq. (42) with the phase constraints in Eq. (43) is that the PR shearogram is directly proportional to the signal changes between the measurement times t_1 and t_4. The resulting scale factor $\mathbf{K}$ in Eq. (46) is immaterial—the output of the algorithm can be scaled to whatever units are convenient—such as waves, radians, or meters of ground motion. Unlike the conventional PS method embodied in Eq. (32), the signs of small signal phases are preserved, without the processing-intensive phase-unwrapping required by arctangent operations. In addition, computation of only one shearogram is required, reducing both noise and computational burden.

The main interest of our work is in identifying hidden structures and defects, for which a shearogram or a sequence of shearograms is sufficient. There may also be applications for which the absolute phase change is desired, in addition to phase differences across a shear field. The PR shearograms provide the relevant data for subsequent processing for such cases. For the example of a vibrating surface, from Eq. (20), we have

$$\varphi_{\mathrm{Signal}}(\mathbf{r},\Delta\mathbf{r}_{\mathrm{Shear}},t_j)=\tfrac{4\pi}{\lambda}\times[h(\mathbf{r}+\Delta\mathbf{r}_{\mathrm{Shear}},t_j)-h(\mathbf{r},t_j)]$$

so that the shearogram is

$$\begin{aligned}&\mathbf{Shearogram}_{\mathrm{PR}}(\mathbf{r},t_1,t_4)\\&\quad\approx\mathbf{K}.*[\sin\boldsymbol{\phi}_{\mathrm{Signal}}(4)-\sin\boldsymbol{\phi}_{\mathrm{Signal}}(1)]\\&\quad\approx\mathbf{K}.*[\boldsymbol{\phi}_{\mathrm{Signal}}(4)-\boldsymbol{\phi}_{\mathrm{Signal}}(1)]\\&\quad\approx\left(\frac{4\pi}{\lambda}\mathbf{K}\right).\\&\quad*[\mathbf{h}(\mathbf{r}+\Delta\mathbf{r}_{\mathrm{Shear}},t_4)-\mathbf{h}(\mathbf{r},t_4)-\mathbf{h}(\mathbf{r}+\Delta\mathbf{r}_{\mathrm{Shear}},t_1)+\mathbf{h}(\mathbf{r},t_1)]\\&\quad\approx\left(\frac{4\pi}{\lambda}\mathbf{K}\right).*\{[\mathbf{h}(\mathbf{r}+\Delta\mathbf{r}_{\mathrm{Shear}},t_4)-\mathbf{h}(\mathbf{r}+\Delta\mathbf{r}_{\mathrm{Shear}},t_1)]\\&\quad-[\mathbf{h}(\mathbf{r},t_4)-\mathbf{h}(\mathbf{r},t_1)]\}.\end{aligned}\tag{49}$$

We now define a temporal strain field as

$$\boldsymbol{\varepsilon}_{\mathrm{Strain}}(t_1,t_4)=[\mathbf{h}(t_4)-\mathbf{h}(t_1)],\tag{50}$$

where we have dropped the explicit reference to the loci. If the shearing field $\Delta\mathbf{r}_{\mathrm{Shear}}$ is a simple linear displacement of the entire image, then the shear is separable in the row and column directions and can be represented by a pair of matrices $\mathbf{S}_L$ and $\mathbf{S}_R$ operating to the left and right sides of the strain field so that

$$\begin{aligned}\mathbf{Shearogram}_{PR}(t_1,t_4)&\approx\left(\frac{4\pi}{\lambda}\mathbf{K}\right).\\&*[\mathbf{S}_L\boldsymbol{\varepsilon}_{\mathrm{Strain}}(t_1,t_4)\mathbf{S}_R-\boldsymbol{\varepsilon}_{\mathrm{Strain}}(t_1,t_4)].\end{aligned}\tag{51}$$

Applying one of the various regularized pseudoinversion methods to Eq. (51) then yields the temporal strain field $\boldsymbol{\varepsilon}_{\mathrm{Strain}}(t_1,t_4)$, to within a global constant. If there are points (such as clamped edges) at which the absolute strain is known, the global constant can be determined, and the absolute strain computed for the entire image. Analysis of the performance of pseudoinverting Eq. (51) to obtain time-dependent strain field $\boldsymbol{\varepsilon}_{\mathrm{Strain}}(t_1,t_4)$ is a topic for future research.

Multiple choices for the intermediate phase steps are possible, consistent with Eq. (43). For a linearly actuated constant-speed phase-shifting element (such as in Fig. 1) and a laser with constant pulse repetition rate, the practical implementation is eased by choosing equal steps in phase, such that

$$\begin{aligned}\boldsymbol{\phi}_{\mathrm{Step}}(1)=0,\quad\boldsymbol{\phi}_{\mathrm{Step}}(2)=2\pi/3,\quad\boldsymbol{\phi}_{\mathrm{Step}}(3)\\=4\pi/3,\quad\text{and}\quad\boldsymbol{\phi}_{\mathrm{Step}}(4)=2\pi.\end{aligned}\tag{52}$$

With Eq. (52) choice of steps, the PR shearogram gives

$$\begin{aligned}\mathbf{Shearogram}_{\mathbf{PR}}&=\frac{[\mathbf{S}(4)-\mathbf{S}(1)]}{[\mathbf{S}(2)-\mathbf{S}(3)]}\\&\approx\frac{1}{\sqrt{3}}[\sin\boldsymbol{\phi}_{\mathrm{Signal}}(4)-\sin\boldsymbol{\phi}_{\mathrm{Signal}}(1)].\end{aligned}\tag{53}$$

The PR processing can also be applied continuously, for example, computing $\mathbf{Shearogram}_{PR}$ for four shots with phases $(0,+2\pi/3,+4\pi/3,0)$ at times $(0,\Delta t,2\Delta t,3\Delta t)$, then four shots with phases $(+2\pi/3,+4\pi/3,0,+2\pi/3)$ at times $(\Delta t,2\Delta t,3\Delta t,4\Delta t)$, then four shots with phases $(+4\pi/3,0,+2\pi/3,+4\pi/3)$ at times $(2\Delta t,3\Delta t,4\Delta t,5\Delta t)$, etc., to produce a continuous movie of the surface motion. The preservation of both the amplitude and the phase of the motion facilitates backpropagation analysis, for example, to infer the locations of sources and scatters.

The only drawback to choosing the phase steps in Eq. (52) is that for large signals, $\mathbf{Shearogram}_{\mathbf{PR}}$ will yield signal estimates that are biased between positive and negative values. An unbiased estimator is provided by instead choosing phase steps of

$$\begin{aligned}\boldsymbol{\phi}_{\mathrm{Step}}(1)=0,\quad\boldsymbol{\phi}_{\mathrm{Step}}(2)=\pi/2,\quad\boldsymbol{\phi}_{\mathrm{Step}}(3)\\=3\pi/2,\quad\text{and}\quad\boldsymbol{\phi}_{\mathrm{Step}}(4)=2\pi,\end{aligned}\tag{54}$$

so that

$$\begin{aligned}\mathbf{Shearogram}_{\mathbf{PR}}&=\frac{[\mathbf{S}(4)-\mathbf{S}(1)]}{[\mathbf{S}(2)-\mathbf{S}(3)]}\\&\approx\frac{1}{2}[\sin\boldsymbol{\phi}_{\mathrm{Signal}}(4)-\sin\boldsymbol{\phi}_{\mathrm{Signal}}(1)].\end{aligned}\tag{55}$$

The application of Eq. (54) entails the complication of an unequal rate of phase stepping with time but provides an unbiased estimate, so we designate it as the unbiased sequence.

To summarize this overview: we have reviewed two commonly used shearography methods: NPS shearography from one shearogram using two shots, Eq. (22), and conventional PS shearography from two shearograms with six to eight shots, Eq. (32). We have also touched on a variation, spatially multiplexed conventional PS shearography from two shearograms using two shots at reduced resolution, Eq. (32). We then presented a new method, PR shearography that creates one shearogram from four shots collected asynchronously with the acoustic excitation, Eq. (53). The asynchronous operation of PR shearography removes a limiter of other PS methods, such as the need to collect four shearograms simultaneously (which limits resolution and $f/\#$), or to hold the system stationary for all four laser pulses (which limits coverage rate), or to synchronize the laser pulses with the phase of the surface motion (impossible in many applications).

PR shearography is the subject of US Patent # 9476700[5] and other patents in process, and its application and exploitation in airborne systems is facilitated by several additional shearography innovations.[6–9]

To compare the performance of the various shearography methods, we compute their noise characteristics, outlined in the following section.

3 Noise Analysis

The dominant noise source in shearography is laser speckle, which cannot be ameliorated by strategies such as increasing laser power or cooling the optics, that reduce other noise sources such as photon-counting noise or dark noise. Thus, the noise analysis in this paper focuses on the speckle noise.

Extensions to the other noise sources will be presented in future publications.

The noise statistic compute here is the full-width at half-maximum (FWHM) of the probability distribution of signal phase inferred from each shearography method.

3.1 *Basic Two-Shot Shearography Speckle Noise*

The statistics of the NPR shearogram $\mathbf{Shearogram_{NPR}}$ can be derived from the PDFs, Eq. (11), of the intensities and the PDF, Eq. (10), of the random speckle phase difference $\boldsymbol{\phi}_{\mathrm{Speckle}}$:

$$\begin{aligned}\mathbf{Shearogram_{NPR}} &= [\mathbf{S}(2) - \mathbf{S}(1)] \\ &= -|\mathbf{E}_0|.*|\mathbf{E}_{\Delta\mathbf{r}}|. \\ &\quad * \left\{ \begin{array}{l} -(\cos\boldsymbol{\phi}_{\mathrm{Speckle}}).*[\cos\boldsymbol{\phi}_{\mathrm{Signal}}(2) - \cos\boldsymbol{\phi}_{\mathrm{Signal}}(1)] \\ +(\sin\boldsymbol{\phi}_{\mathrm{Speckle}}).*[\sin\boldsymbol{\phi}_{\mathrm{Signal}}(2) - \sin\boldsymbol{\phi}_{\mathrm{Signal}}(1)] \end{array} \right\} \\ &\approx -|\mathbf{E}_0|.*|\mathbf{E}_{\Delta\mathbf{r}}|.*\sin\boldsymbol{\phi}_{\mathrm{Speckle}}. \\ &\quad *[\sin\boldsymbol{\phi}_{\mathrm{Signal}}(2) - \sin\boldsymbol{\phi}_{\mathrm{Signal}}(1)]. \end{aligned} \tag{56}$$

The ratio of the measured shearogram to the input signal change is

$$\begin{aligned}\mathbf{R_{NPR}} &= \frac{\mathbf{Shearogram_{NPR}}}{[\sin\boldsymbol{\phi}_{\mathrm{Signal}}(1) - \sin\boldsymbol{\phi}_{\mathrm{Signal}}(2)]} \\ &= |\mathbf{E}_0|.*|\mathbf{E}_{\Delta\mathbf{r}}|.*\sin\boldsymbol{\phi}_{\mathrm{Speckle}}. \end{aligned} \tag{57}$$

To compute the statistics of $\mathbf{R_{NPR}}$, we first perform a coordinate transformation from $(\sin\boldsymbol{\phi}_{\mathrm{Speckle}}, |\mathbf{E}_0|.*|\mathbf{E}_{\Delta\mathbf{r}}|)$ to $(\mathbf{R_{NPR}}, |\mathbf{E}_0|, |\mathbf{E}_{\Delta\mathbf{r}}|)$, using the Jacobian of the transformation, then integrate over the variables $|\mathbf{E}_0|$ and $|\mathbf{E}_{\Delta\mathbf{r}}|$ to get the PDF $\mathbf{P}(\mathbf{R_{NPR}})$:

$$\mathbf{P}(\mathbf{R_{NPR}}) = \int_0^\infty \mathrm{d}|\mathbf{E}_0| \int_0^\infty \mathrm{d}|\mathbf{E}_{\Delta\mathbf{r}}| \mathbf{P}(\mathbf{R_{NPR}}, |\mathbf{E}_0|, |\mathbf{E}_{\Delta\mathbf{r}}|). \tag{58}$$

The coordinate transformation gives

$$\begin{aligned}\mathbf{P}(\mathbf{R_{NPR}}, |\mathbf{E}_0|, |\mathbf{E}_{\Delta\mathbf{r}}|) &= \mathbf{P}(\sin\boldsymbol{\phi}_{\mathrm{Speckle}}).*\mathbf{P}(|\mathbf{E}_0|).*\mathbf{P}(|\mathbf{E}_{\Delta\mathbf{r}}|). \\ &\quad * \left\| \begin{matrix} \frac{\partial\sin\boldsymbol{\phi}_{\mathrm{Speckle}}}{\partial\mathbf{R_{NPR}}} & \frac{\partial|\mathbf{E}_0|}{\partial\mathbf{R_{NPR}}} & \frac{\partial|\mathbf{E}_{\Delta\mathbf{r}}|}{\partial\mathbf{R_{NPR}}} \\ \frac{\partial\sin\boldsymbol{\phi}_{\mathrm{Speckle}}}{\partial|\mathbf{E}_0|} & \frac{\partial|\mathbf{E}_0|}{\partial|\mathbf{E}_0|} & \frac{\partial|\mathbf{E}_{\Delta\mathbf{r}}|}{\partial|\mathbf{E}_0|} \\ \frac{\partial\sin\boldsymbol{\phi}_{\mathrm{Speckle}}}{\partial|\mathbf{E}_{\Delta\mathbf{r}}|} & \frac{\partial|\mathbf{E}_0|}{\partial|\mathbf{E}_{\Delta\mathbf{r}}|} & \frac{\partial|\mathbf{E}_{\Delta\mathbf{r}}|}{\partial|\mathbf{E}_{\Delta\mathbf{r}}|} \end{matrix} \right\| \\ &= \mathbf{P}(\sin\boldsymbol{\phi}_{\mathrm{Speckle}}).*\mathbf{P}(|\mathbf{E}_0|).*\mathbf{P}(|\mathbf{E}_{\Delta\mathbf{r}}|).*\frac{\partial\sin\boldsymbol{\phi}_{\mathrm{Speckle}}}{\partial\mathbf{R_{NPR}}} \\ &= \mathbf{P}(\sin\boldsymbol{\phi}_{\mathrm{Speckle}}).*[\mathbf{P}(|\mathbf{E}_0|)./|\mathbf{E}_0|].*[\mathbf{P}(|\mathbf{E}_{\Delta\mathbf{r}}|)./|\mathbf{E}_{\Delta\mathbf{r}}|], \end{aligned} \tag{59}$$

with the values of $\sin\boldsymbol{\phi}_{\mathrm{Speckle}}$ evaluated at

$$\sin\boldsymbol{\phi}_{\mathrm{Speckle}} = \mathbf{R_{NPR}}./(|\mathbf{E}_0|.*|\mathbf{E}_{\Delta\mathbf{r}}|). \tag{60}$$

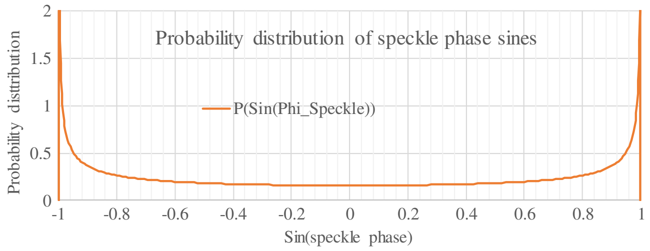

Fig. 2 Probability distribution in Eq. (61). While the mean value is zero, the most likely values are singularities at $\sin\boldsymbol{\phi}_{\mathrm{Speckle}} = \pm 1$, presenting a large noise source for speckle imaging.

PDF of $(\sin\boldsymbol{\phi}_{\mathrm{Speckle}})$ is

$$\begin{aligned}\mathbf{P}(\sin\boldsymbol{\phi}_{\mathrm{Speckle}}) &= \mathbf{P}(\boldsymbol{\phi}_{\mathrm{Speckle}})(\partial\boldsymbol{\phi}_{\mathrm{Speckle}}/\partial\sin\boldsymbol{\phi}_{\mathrm{Speckle}}) \\ &= \frac{1}{2\pi\sqrt{1-\sin^2\boldsymbol{\phi}_{\mathrm{Speckle}}}}. \end{aligned} \tag{61}$$

On the interval* $-\pi/2 < \boldsymbol{\phi}_{\mathrm{Speckle}} < +\pi/2$, Eq. (61) gives a "cat ears" distribution with integrable singularities at $\sin\boldsymbol{\phi}_{\mathrm{Speckle}} = \pm 1$, as shown in Fig. 2. Thus, while the mean value of $\sin\boldsymbol{\phi}_{\mathrm{Speckle}}$ is zero, the most likely values are the extremes ± 1.

Substituting Eqs. (59)–(61), into Eq. (58) gives

$$\begin{aligned}\mathbf{P}(\mathbf{R_{NPR}}) &= \int_0^\infty \mathrm{d}|\mathbf{E}_0| \int_0^\infty \mathrm{d}|\mathbf{E}_{\Delta\mathbf{r}}| \mathbf{P}(\mathbf{R_{NPR}}, |\mathbf{E}_0|, |\mathbf{E}_{\Delta\mathbf{r}}|) \\ &= \frac{1}{\sqrt{\langle\mathbf{I}_0\rangle.*\langle\mathbf{I}_{\Delta\mathbf{r}}\rangle}}.*\exp\left[-2\frac{|\mathbf{R_{NPR}}|}{\sqrt{\langle\mathbf{I}_{\Delta\mathbf{r}}\rangle.*\langle\mathbf{I}_0\rangle}}\right]. \end{aligned} \tag{62}$$

The mean and most likely values of $\mathbf{R_{NPR}}$ are always zero, although it is unbounded, ranging between $\pm\infty$. The signals of interest are $|\mathbf{X}_{\mathrm{NPR}}|$, given as

$$\begin{aligned}|\mathbf{X}_{\mathrm{NPR}}| &= 2|\mathbf{Shearogram_{NPR}}|./\sqrt{\langle\mathbf{I}_{\Delta\mathbf{r}}\rangle.*\langle\mathbf{I}_0\rangle} \\ &= 2([\sin\boldsymbol{\phi}_{\mathrm{Signal}}(1) - \sin\boldsymbol{\phi}_{\mathrm{Signal}}(2)]./\sqrt{\langle\mathbf{I}_{\Delta\mathbf{r}}\rangle.*\langle\mathbf{I}_0\rangle}). \\ &\quad *\mathbf{R_{NPR}} \\ &= 2\mathbf{X}_0.*\mathbf{R_{NPR}}./\sqrt{\langle\mathbf{I}_{\Delta\mathbf{r}}\rangle.*\langle\mathbf{I}_0\rangle}, \end{aligned} \tag{63}$$

where the "true" input signal is

$$\mathbf{X_0} = |\sin\boldsymbol{\phi}_{\mathrm{Signal}}(1) - \sin\boldsymbol{\phi}_{\mathrm{Signal}}(2)|. \tag{64}$$

The probability distribution for $|\mathbf{X}_{\mathrm{NPR}}|$, derived from $\mathbf{P}(\mathbf{R_{NPR}})$ is

$$\mathbf{P}(\mathbf{X}_{\mathrm{NPR}}) = [\exp(-|\mathbf{X}_{\mathrm{NPR}}|./\mathbf{X_0})]./\mathbf{X_0}. \tag{65}$$

As Fig. 3 shows, regardless of signal level, the most-likely value of $\mathbf{X}_{\mathrm{NPR}}$ is zero, annihilating the signal signs. The FWHM is $2\mathbf{X_0}.*\ln(0.5\mathbf{X_0})$. Equation (63) shows the difficulty of estimating the signal phase from the shearograms

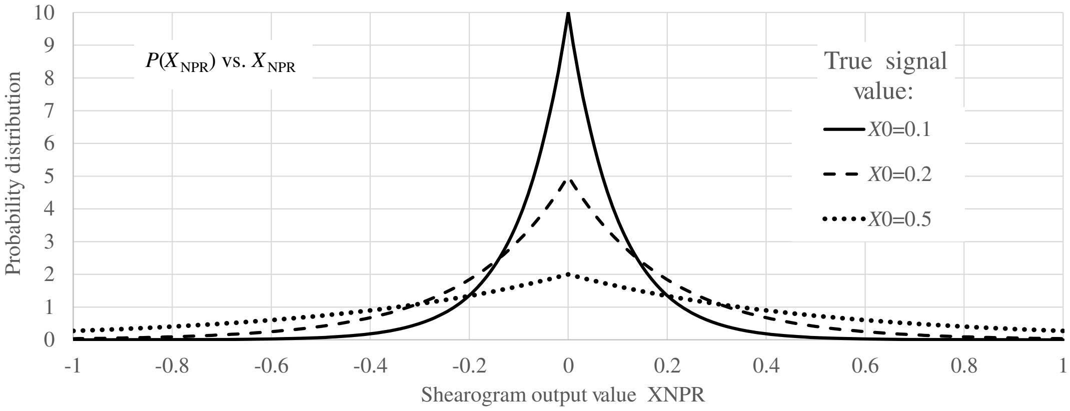

Fig. 3 NPR shearogram-output PDFs from Eq. (65) for various true signals X_0. NPR shearography gives ambiguous sign and always has a most likely value of zero. The true value X_0 is estimated by processing many adjacent shearogram pixels.

since the actual mean signal levels $\langle \mathbf{I}_{\Delta \mathbf{r}} \rangle$ and $\langle \mathbf{I}_0 \rangle$ are often not well known or precisely characterizable. This makes the scaling, from shearograms to signal phases, dependent on postprocessing and various "phase unwrapping" methods. For signals smaller than a wavelength of light, the actual magnitude of the signal is thus indeterminate.

3.2 *Phase-Stepped Shearography Speckle Noise*

Equation (36), together with conservation of probabilities, yields the probability distribution of the estimated PS-shearography signal $\mathbf{X}_{\mathrm{PS}}$ is

$$\mathbf{P}(\mathbf{X}_{\mathrm{PS}}) = \left(1 - \frac{|\mathbf{X}_0|}{2\pi}\right). * \delta(\mathbf{X}_{\mathrm{PS}} - \mathbf{X}_0) + \frac{|\mathbf{X}_0|}{2\pi}. * \begin{Bmatrix} \delta[\mathbf{X}_{\mathrm{PS}} - (-2\pi + \mathbf{X}_0)], & \mathbf{X}_0 > 0 \\ \delta[\mathbf{X}_{\mathrm{PS}} - (2\pi + \mathbf{X}_0)], & \mathbf{X}_0 < 0 \end{Bmatrix}. \tag{66}$$

Because the true range of X_0 and X_{PS} are both $(-\pi, +\pi)$ radians, Eq. (66) can be rectified by adding $\pm 2\pi$ to values outside the valid range so that

$$\mathbf{P}(\mathbf{X}_{\mathrm{PS}}) = \delta(\mathbf{X}_{\mathrm{PS}} - \mathbf{X}_0). \tag{67}$$

In real-world applications, other sources of noise blur the PDFs. Resolving the ambiguities requires processing groups of adjacent pixels, using various processing methods.[10]

3.3 *Phase-Resolved Shearography Speckle Noise*

The error ranges in the present method arise from the terms containing elements proportional to $\boldsymbol{\phi}_{\mathrm{Speckle}}$. In the general case for finite amplitudes is derived from Eqs. (42) and (43), and for $\mathrm{Shear}_{\mathrm{PR\_1}}$ yields

$$\mathbf{Shearogram}_{\mathrm{PR}} = \frac{[(\mathbf{S4}) - (\mathbf{S1})]}{[(\mathbf{S2}) - (\mathbf{S3})]} \approx \frac{\mathbf{S}_{4,1} - \mathbf{C}_{4,1}. * \cot \boldsymbol{\phi}_{\mathrm{Speckle}}}{\mathbf{S}_{3,2} - \mathbf{C}_{3,2}. * \cot \boldsymbol{\phi}_{\mathrm{Speckle}}}, \tag{68}$$

where

$$\mathbf{C}_{4,1} = [\cos \boldsymbol{\phi}_{\mathrm{Signal}}(4) - \cos \boldsymbol{\phi}_{\mathrm{Signal}}(1)],$$
$$\mathbf{S}_{4,1} = [\sin \boldsymbol{\phi}_{\mathrm{Signal}}(4) - \sin \boldsymbol{\phi}_{\mathrm{Signal}}(1)],$$
$$\mathbf{C}_{3,2} = \begin{Bmatrix} [\cos \boldsymbol{\phi}_{\mathrm{Signal}}(2) - \cos \boldsymbol{\phi}_{\mathrm{Signal}}(3)]. * \cos \boldsymbol{\phi}_{\mathrm{Step}}(2) \\ -[\sin \boldsymbol{\phi}_{\mathrm{Signal}}(2) + \sin \boldsymbol{\phi}_{\mathrm{Signal}}(3)]. * \sin \boldsymbol{\phi}_{\mathrm{Step}}(2) \end{Bmatrix},$$

and

$$\mathbf{S}_{3,2} = \begin{Bmatrix} [\sin \boldsymbol{\phi}_{\mathrm{Signal}}(2) - \sin \boldsymbol{\phi}_{\mathrm{Signal}}(3)]. * \cos \boldsymbol{\phi}_{\mathrm{Step}}(2) \\ +[\cos \boldsymbol{\phi}_{\mathrm{Signal}}(2) + \cos \boldsymbol{\phi}_{\mathrm{Signal}}(3)]. * \sin \boldsymbol{\phi}_{\mathrm{Step}}(2) \end{Bmatrix}. \tag{69}$$

The PDF for Eq. (68) is derived from conservation of probabilities

$$P(\mathbf{Shearogram}_{\mathrm{PR}}) = P(\cot \boldsymbol{\phi}_{\mathrm{Speckle}}). * \frac{\partial(\cot \boldsymbol{\phi}_{\mathrm{Speckle}})}{\partial \mathbf{Shearogram}_{\mathrm{PR}}}, \tag{70}$$

evaluated at

$$\cot \boldsymbol{\phi}_{\mathrm{Speckle}} = \frac{[\mathbf{S}_{4,1} - \mathbf{S}_{3,2}. * \mathbf{Shearogram}_{\mathrm{PR}}]}{[\mathbf{C}_{4,1} - \mathbf{C}_{3,2}. * \mathbf{Shearogram}_{\mathrm{PR}}]}. \tag{71}$$

Substituting

$$P(\cot \boldsymbol{\phi}_{\mathrm{Speckle}}) = \frac{1}{\pi} \frac{\partial \boldsymbol{\phi}_{\mathrm{Speckle}}}{\partial(\cot \boldsymbol{\phi}_{\mathrm{Speckle}})} = \frac{1}{\pi} \left[\frac{1}{1 + (\cot \boldsymbol{\phi}_{\mathrm{Speckle}})^2}\right], \tag{72}$$

and

$$\frac{\partial(\cot \boldsymbol{\phi}_{\mathrm{Speckle}})}{\partial \mathbf{Shearogram}_{\mathrm{PR}}} = \frac{[\mathbf{C}_{3,2}. * \mathbf{S}_{4,1} - \mathbf{S}_{3,2}. * \mathbf{C}_{4,1}]}{[\mathbf{C}_{4,1} - \mathbf{C}_{3,2}. * \mathbf{Shearogram}_{\mathrm{PR}}]^2}, \tag{73}$$

into Eq. (70) yields the probability distribution for the signal-change estimate $\mathbf{X_{PR}}$

$$\mathbf{P}(\mathbf{X}_{\mathrm{PR}}) = \frac{1}{\pi} \frac{\mathbf{W}}{[(\mathbf{X}_{\mathrm{PR}} - \mathbf{X}_{\mathrm{ML}})^2 + \mathbf{W}^2]}, \tag{74}$$

where

$$\mathbf{X}_{\mathrm{PR}} = \mathbf{Shearogram}_{\mathrm{PR}}. * \sqrt{\mathbf{C}_{3,2}^2 + \mathbf{S}_{3,2}^2}, \tag{75}$$

$$\mathbf{X}_{\mathrm{ML}}=[\mathbf{C}_{3,2}.*\mathbf{C}_{4,1}+\mathbf{S}_{3,2}.*\mathbf{S}_{4,1}]./\sqrt{\mathbf{C}_{3,2}^2+\mathbf{S}_{3,2}^2}, \tag{76}$$

and

$$\mathbf{W}^2=[\mathbf{C}_{4,1}.*\mathbf{S}_{3,2}-\mathbf{C}_{3,2}.*\mathbf{S}_{4,2}]^2./[\mathbf{C}_{3,2}^2+\mathbf{S}_{3,2}^2]. \tag{77}$$

Equation (74) is a Cauchy-type distribution for $\mathbf{X}_{\mathrm{PR}}$, symmetrically distributed about the most-likely vector $\mathbf{X}_{\mathrm{PR=XML}}$, with width-parameter vector $\mathbf{W}$. The most-likely value is also the median of the distribution, and the FWHM equals $2\mathbf{W}$. As the signal levels become small, the parameters in Eq. (77) have the limits

$$\mathbf{X}_{\mathrm{ML}}\underset{\text{small signal}}{\rightarrow}[\boldsymbol{\phi}_{\mathrm{Signal}}(4)-\boldsymbol{\phi}_{\mathrm{Signal}}(1)]=\mathbf{X}_0,\ \text{and}$$
$$\mathbf{W}\underset{\text{small signal}}{\rightarrow}\frac{1}{2}|[\boldsymbol{\phi}_{\mathrm{Signal}}(2)+\boldsymbol{\phi}_{\mathrm{Signal}}(3)][\boldsymbol{\phi}_{\mathrm{Signal}}(4)-\boldsymbol{\phi}_{\mathrm{Signal}}(1)]|. \tag{78}$$

Thus, even though the distribution's variance is undefined, the widths $\mathbf{W}$ of the distribution fall to zero faster than the medians $\mathbf{X}_{\mathrm{ML}}$ as the signals approach zero, allowing exquisite sensitivity to small signal phases.

For the general case of nonsmall signal phases with the unbiased sequence of phase steps in Eq. (54), the width parameter reduces to

$$\mathbf{W}_{\mathrm{unbiased}}=\frac{\left\{\begin{matrix}\cos[\boldsymbol{\phi}_{\mathrm{Signal}}(4)-\boldsymbol{\phi}_{\mathrm{Signal}}(2)]+\cos[\boldsymbol{\phi}_{\mathrm{Signal}}(4)-\boldsymbol{\phi}_{\mathrm{Signal}}(3)]\\-\cos[\boldsymbol{\phi}_{\mathrm{Signal}}(1)-\boldsymbol{\phi}_{\mathrm{Signal}}(2)]-\cos[\boldsymbol{\phi}_{\mathrm{Signal}}(1)-\boldsymbol{\phi}_{\mathrm{Signal}}(3)]\end{matrix}\right\}^{1/2}}{\{2+2\cos[\boldsymbol{\phi}_{\mathrm{Signal}}(3)-\boldsymbol{\phi}_{\mathrm{Signal}}(2)]\}^{1/2}}, \tag{79}$$

and the most-likely value becomes

$$\mathbf{X}_{\mathrm{ML,unbiased}}=\frac{\left\{\begin{matrix}\sin[\boldsymbol{\phi}_{\mathrm{Signal}}(4)-\boldsymbol{\phi}_{\mathrm{Signal}}(2)]+\sin[\boldsymbol{\phi}_{\mathrm{Signal}}(4)-\boldsymbol{\phi}_{\mathrm{Signal}}(3)]\\+\sin[\boldsymbol{\phi}_{\mathrm{Signal}}(3)-\boldsymbol{\phi}_{\mathrm{Signal}}(1)]+\sin[\boldsymbol{\phi}_{\mathrm{Signal}}(2)-\boldsymbol{\phi}_{\mathrm{Signal}}(1)]\end{matrix}\right\}}{\{2+2\cos[\boldsymbol{\phi}_{\mathrm{Signal}}(3)-\boldsymbol{\phi}_{\mathrm{Signal}}(2)]\}^{1/2}}. \tag{80}$$

In the special case of a linear variation of signal phase with time, the signal phase differences are equal in each time interval so that the width $\mathbf{W}_{\text{quarter-steps}}\Rightarrow 0$, even for large signals, and the PDF becomes a delta function at the most-likely values $\mathbf{X}_{\mathrm{ML,unbiased}}$:

$$\mathbf{X}_{\mathrm{ML,unbiased}}\Rightarrow\sqrt{2}\left[\sin\left(\frac{2}{3}\mathbf{X}_0\right)+\sin\left(\frac{1}{3}\mathbf{X}_0\right)\right]\Big/\left[1+\cos\left(\frac{1}{3}\mathbf{X}_0\right)\right]^{1/2}. \tag{81}$$

For $\mathbf{X}_0$ in the interval $(-\pi,+\pi)$, Eq. (81) is monotonic and smoothly varying, and thus numerically invertible to yield an unbiased estimate of $\mathbf{X}_0$ so that for linear signal variation with time (or for small signals with any time dependence):

$$\mathbf{P}(\mathbf{X}_{\mathrm{PR,debiased}})=\delta(\mathbf{X}_{\mathrm{PR,debiased}}-\mathbf{X}_0). \tag{82}$$

3.4 *Phase-Resolved Statistics with 2π/3 Steps*

For a many-shot sequence, synchronizing phase steps produced by a moving phase-element with a pulsed laser is greatly facilitated if the phase steps are equally spaced in $1/3$-wave steps of sequence Eq. (52) $(0,2\pi/3,4\pi/3,2\pi,\dots)$ rather than the unequal intervals $(0,\pi/2,3\pi/2,2\pi,\dots)$. In this case, Eq. (69) gives

$$\begin{aligned}\mathbf{C}_{4,1}&=[\cos\boldsymbol{\phi}_{\mathrm{Signal}}(4)-\cos\boldsymbol{\phi}_{\mathrm{Signal}}(1)],\\ \mathbf{S}_{4,1}&=[\sin\boldsymbol{\phi}_{\mathrm{Signal}}(4)-\sin\boldsymbol{\phi}_{\mathrm{Signal}}(1)],\\ \mathbf{C}_{3,2}&=\frac{1}{2}\Big\{-\sqrt{3}[\cos\boldsymbol{\phi}_{\mathrm{Signal}}(2)-\cos\boldsymbol{\phi}_{\mathrm{Signal}}(3)]\\&\quad-[\sin\boldsymbol{\phi}_{\mathrm{Signal}}(2)+\sin\boldsymbol{\phi}_{\mathrm{Signal}}(3)]\Big\},\ \text{and}\\ \mathbf{S}_{3,2}&=\frac{1}{2}\Big\{[\sin\boldsymbol{\phi}_{\mathrm{Signal}}(2)-\sin\boldsymbol{\phi}_{\mathrm{Signal}}(3)]\\&\quad-\sqrt{3}[\cos\boldsymbol{\phi}_{\mathrm{Signal}}(2)+\cos\boldsymbol{\phi}_{\mathrm{Signal}}(3)]\Big\}.\end{aligned} \tag{83}$$

Figure 4 shows PDFs from Eq. (74) for several cases, obtained by substituting Eq. (83) into Eqs. (76) and (77). This case is for a linear phase variation over time, with $\mathbf{X}_0=[\boldsymbol{\phi}_{\mathrm{Signal}}(4)-\boldsymbol{\phi}_{\mathrm{Signal}}(1)]$.

Unlike the unbiased optimal sequence, Eq. (54), the equal-step values in Eq. (52) give widths that do not vanish identically for linear signal ramps, though they still go to zero as the signal levels become small. Thus, there is a trade-off between mechanical simplicity and surface-vibration sensitivity in selecting step sequences for PR shearography.

For linear ramps, Eq. (83) reduce to

$$\begin{aligned}\mathbf{C}_{4,1}&=[\cos(\mathbf{X}_0)-1],\quad \mathbf{S}_{4,1}=\sin(\mathbf{X}_0),\\ \mathbf{C}_{3,2}&=\frac{1}{2}\Big\{-\sqrt{3}[\cos(\mathbf{X}_0/3)-\cos(2\mathbf{X}_0/3)]\\&\quad-[\sin(\mathbf{X}_0/3)+\sin(2\mathbf{X}_0/3)]\Big\},\ \text{and}\\ \mathbf{S}_{3,2}&=\frac{1}{2}\Big\{[\sin(\mathbf{X}_0/3)-\sin(2\mathbf{X}_0/3)]-\sqrt{3}[\cos(\mathbf{X}_0/3)\\&\quad+\cos(2\mathbf{X}_0/3)]\Big\}.\end{aligned} \tag{84}$$

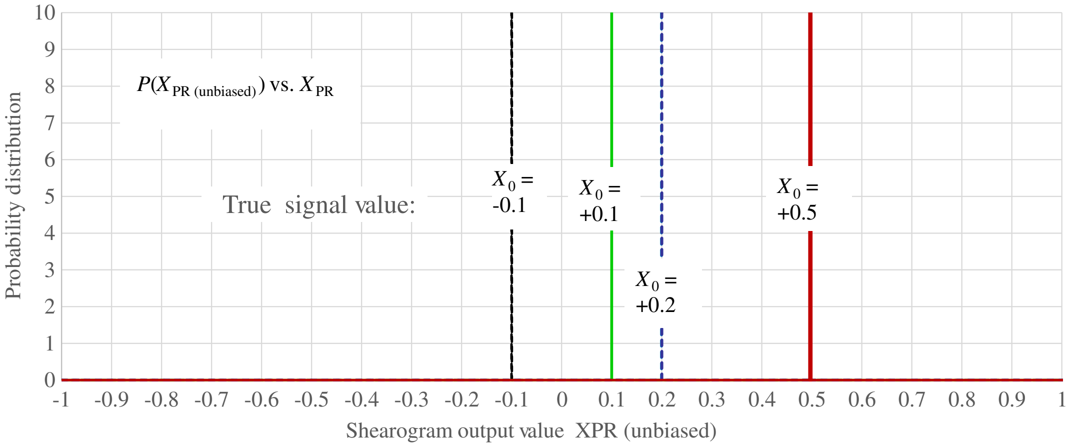

Fig. 4 PR shearogram-output PDFs from Eq. (74) for various true signals X_0. PR shearography resolves the signs of the true signal and has most-likely values (the peaks of the PDFs) at or near the true values of X_0. In this case, the true phase varies linearly with time so that the PDFs are delta functions, in accord with Eq. (82).

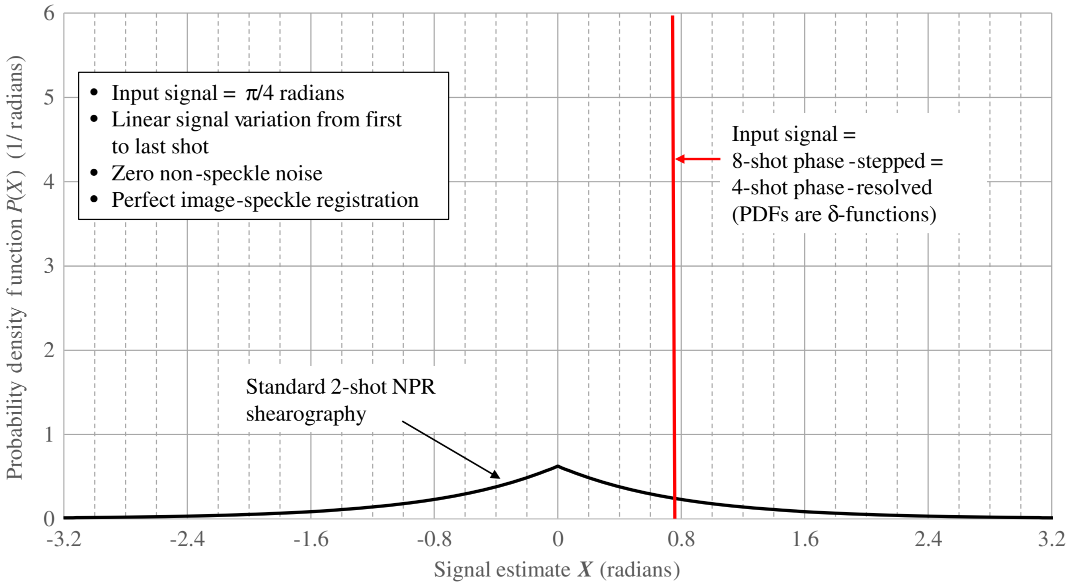

Fig. 5 Comparison of PDFs for two-shot NPR shearography Eq. (65), standard PS shearography Eq. (67), and PR shearography Eq. (82). Under ideal speckle-noise-only conditions, both PS and PR shearography perfectly reconstruct the input signal, whereas NPR shearography yields an exponential distribution with indeterminate sign. Both the PS and PR shearography used phase steps of $(0, \pi/2, 3\pi/2, 2\pi)$ radians.

3.5 *Speckle Statistics Summary*

Figure 5 graphs the PDFs for the various shearography methods. The perfect signal reconstructions of the PS and PR methods rely on speckle persistence during the image-acquisition time, the exact speckle registration between images, and the absence of nonspeckle noise sources.

Figure 6 compares PDF examples for NPR shearography to PR shearography for two different phase-step sequences: the unbiased sequence $(0, \pi/2, 3\pi/2, 2\pi)$ radians and the equal-phase sequence $(0, 2\pi/3, 4\pi/3, 2\pi)$ radians. In this example, the true signal is relatively large, 0.8 rad ($\approx 1/8$ wave). Both the unbiased and equal-step PR sequences have most-likely values near the true signal value, whereas the NPR shearography has most-likely value of zero. The main difference between the two PR step sequences is in the widths of the distributions—the unbiased distribution approximates a delta function, whereas the equal-time distribution has widths from Eq. (77).

3.6 *Nonspeckle Sources of Noise*

While random laser speckle dominates the noise of shearography systems, other noise sources also contribute, such as photon-counting noise, read noise, dark noise, and fixed-pattern noise. In addition, any electrical or mechanical effects that cause the controlled phase to deviate from the nominal values also introduce noise. Our data and analyses show that these effects interact in nonlinear ways. We have developed system-design and processing strategies that

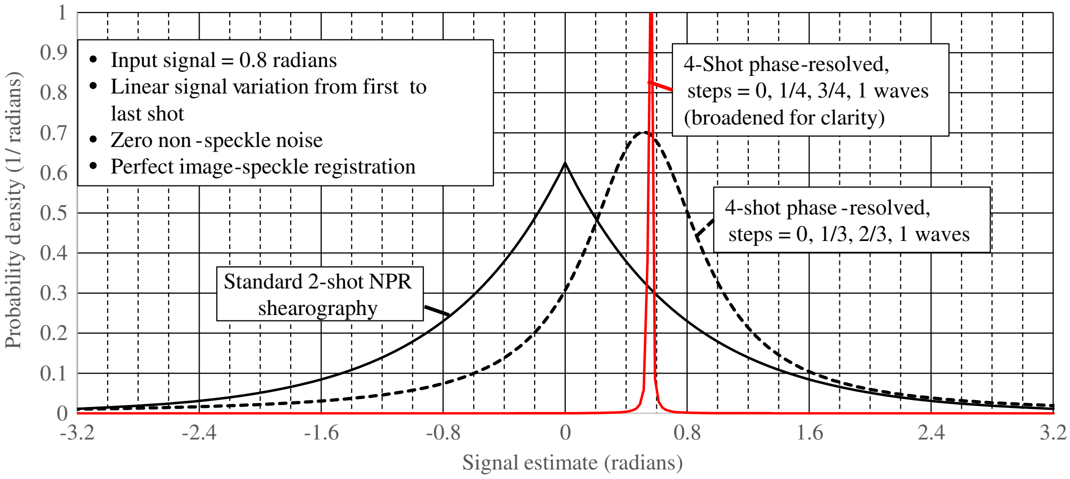

Fig. 6 Comparison of PDFs for two-shot NPR shearography Eq. (65), and PR shearography Eq. (82), for two stepping sequences.

mitigate these noise sources, which will be the subject of future publications.

4 Experimental Confirmation

To test the PR shearography system with a controlled conditions, we constructed a test target with a piezo-electrically actuated deformation. The target was a 0.25-in.-thick aluminum plate with a thinned section. The thinned section was 8 in. (20.3 cm) in diameter and thinned to 0.06in. (1.52 mm). The method of exciting the thinned-aluminum target is shown in Fig. 7. The front of the aluminum plate was covered with custom-fabricated rough surface to provide a laser-reflective surface representative of diffusely reflecting natural surfaces. At the amplitudes studied, the thinned portion is a thick membrane, with deflections described as[11]

$$h(r) = A[1 - (r/a)^2]^2 \quad \text{for } r \geq a, \tag{85}$$

where

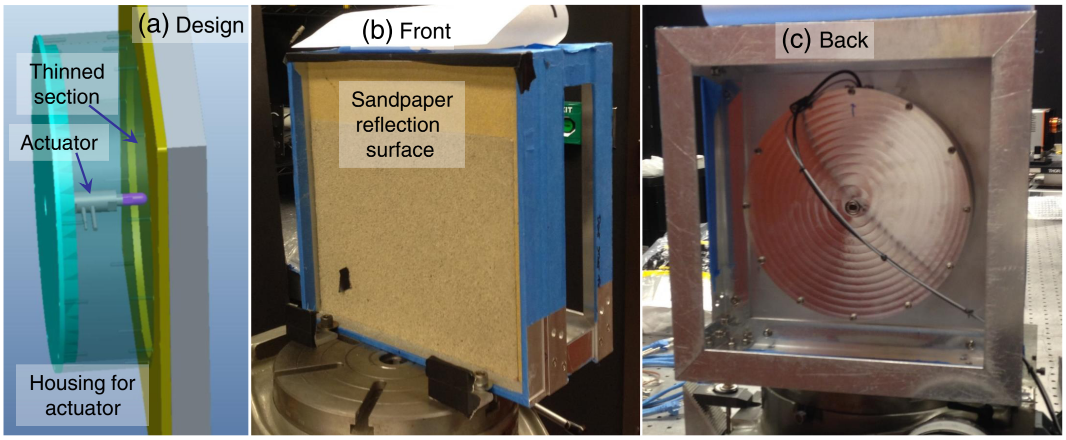

Fig. 7 Laboratory target for shearography experiments.

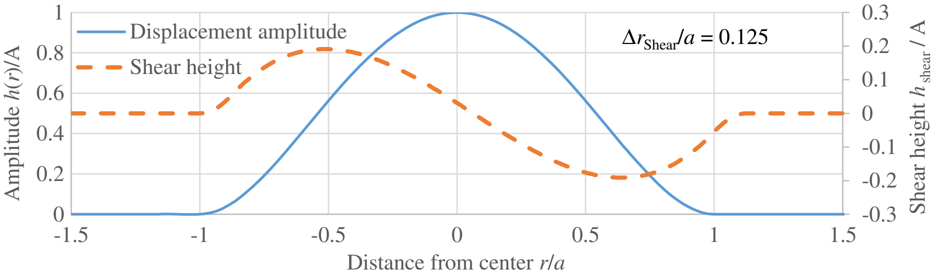

Fig. 8 Displacement amplitude, Eq. (85), and shear height, Eq. (86) for a thick membrane. The shear height is computed for a cut across the center of the image, in the shear direction. In this case, the shear distance at the surface is 1/8 of the membrane radius.

Table 2 Circular-membrane deflection and phase steps for laboratory experiments.

Laser pulse	Membrane deflection at center	Phase step “equal time” sequence	Phase step “unbiased” sequence
1	h_0	0	0
2	$h_0 + A/3$	$\lambda/3$	$\lambda/4$
3	$h_0 + 2A/3$	$2\lambda/3$	$3\lambda/4$
4	$h_0 + A$	λ	Λ

$r =$ distance from center,

$h =$ height of deformation at radius r,

$a =$ radius of membrane $= 4$ in., and

$A = h(0) =$ center deformation amplitude.

The quantity of interest for shearography is the shear height, which is defined as the elevation difference between two points separated by the shear vector. For two points separated by a shear vector $\Delta\mathbf{r}_{\mathrm{Shear}}$ on the membrane described by Eq. (85), the shear distance is

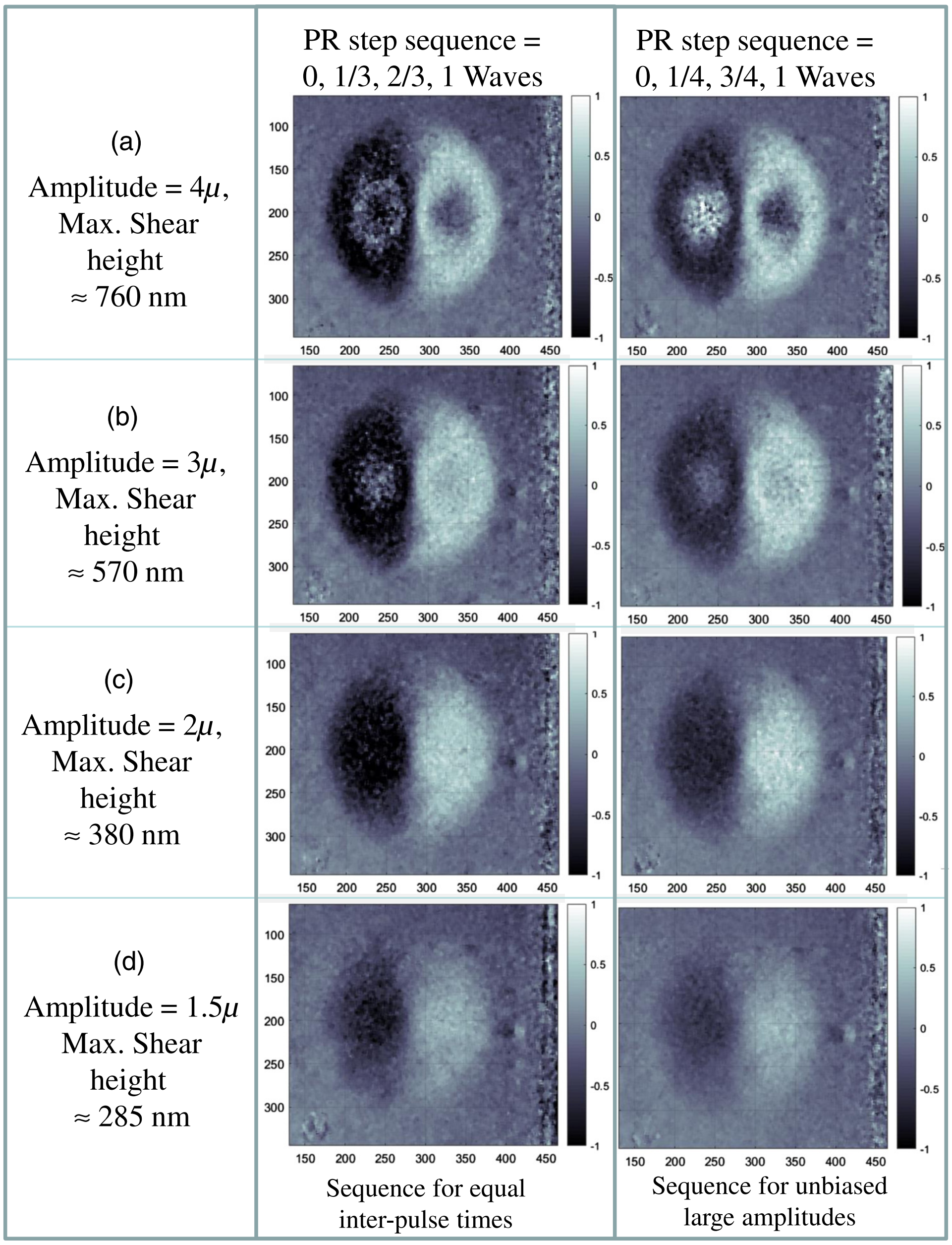

Fig. 9 PR shearograms of a roughened diffusely coated circular-membrane target illuminated with a $\lambda = 1064$ nm laser. Shear height represents the actual sensitivity of the shearography system. (Shear height is the change in displacement over the shear distance between the first and last laser pulse.) Note that for small amplitudes, the sign of the signal is recovered in the raw shearograms, with no additional computational or unwrapping steps. White is positive, black negative, and gray neutral.

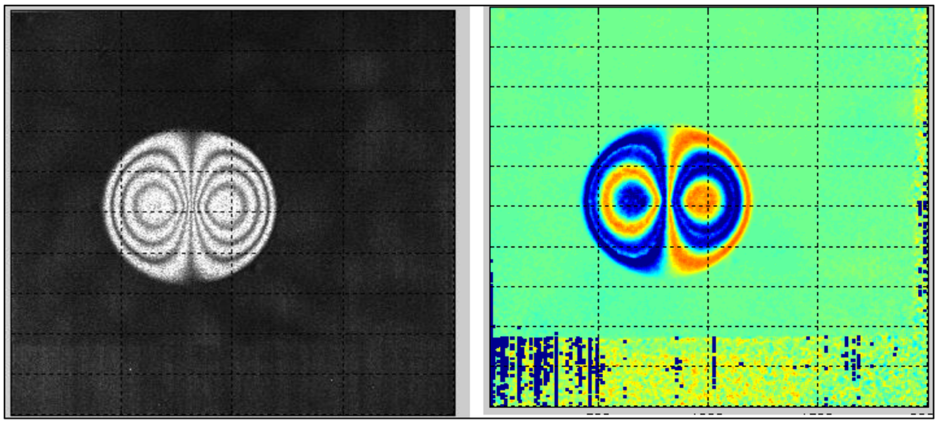
(a) (b)

Fig. 10 (a) “Butterfly” pattern using the basic two-shot shearography method. Only the amplitude of the motion is resolved, not its sign. (b) Tests of PR shearography: blue areas have positive signal (phase-gradient) change, red negative, and green areas were stationary. Because PR shearography can resolve the sign of the surface phase gradient, it gives half as many fringes as NPR shearography. This reduces the need for phase unwrapping for high signal amplitudes and completely eliminates the need for phase unwrapping for low-amplitude signals.

$$h_{\mathrm{Shear}}(\mathbf{r}) = [h(|\mathbf{r}+\Delta\mathbf{r}_{\mathrm{Shear}}|) - h(r)] \\ = A\left\{\left[1-\left(\frac{|\mathbf{r}+\Delta\mathbf{r}_{\mathrm{Shear}}|}{a}\right)^2\right]^2 - \left[1-\left(\frac{r}{a}\right)^2\right]^2\right\}. \tag{86}$$

This can be approximated as

$$h_{\mathrm{Shear}}(\mathbf{r}) \approx \Delta\mathbf{r}_{\mathrm{Shear}} \cdot \nabla h(\mathbf{r}) = A\Delta\mathbf{r}_{\mathrm{Shear}} \cdot \nabla\left[1-\left(\frac{r}{a}\right)^2\right]^2 \\ = 4\left[1-\left(\frac{r}{a}\right)^2\right]\frac{\Delta\mathbf{r}_{\mathrm{Shear}}\cdot\mathbf{r}}{a^2}. \tag{87}$$

The shear height is maximized for $\mathbf{r}$ parallel to the shear direction at the points where $(r/a)^2 = 1/3$, yielding a maximum shear height (from first to last pulse) of

$$h_{\mathrm{Shear,Max}} \approx \frac{8}{3\sqrt{3}}\left(\frac{\Delta r_{\mathrm{Shear}}}{a}\right)A. \tag{88}$$

In these laboratory tests, the range to target was 0.93 m. The camera focal length 25 mm, the laser wavelength λ was 1064 nm, and the shear distance at target was 0.5 in. (1.27 cm). The active portion of the target was 8 in. (20.5 cm) in diameter. The shear distance was kept small because of extreme sensitivity of the membrane to vibrations in the laboratory. For the case $a = 4$ in. and $\Delta r_{\mathrm{Shear}} = 0.5$ in., Eq. (86) gives

$$h_{\mathrm{Shear,Max}} \approx 0.19 \times A, \tag{89}$$

as shown in Fig. 8.

The test-target deformation and the shearography phase-stepping mirror positions were varied as the laser pulsed, to generate PR shearograms with the stepping sequences summarized in Table 2.

PR shearograms are shown in Fig. 9, labeled with the maximum shear heights for each membrane-deflection amplitude. At large shear heights, greater than $\lambda/2$, [(a) and (b)], the equal-time sequence shows a bias between positive (bright) and negative (dark) changes in surface elevation. At low amplitudes ($\ll\lambda$), the biases disappear, and all PR sequences asymptote to the ideal case given by Eq. (78).

Figure 9 shows PR imagery for shear amplitudes of ~0.27 waves of light. This is not the lower limit of resolution. Under ideal conditions, we have achieved ground resolutions (noise equivalent shear height) of 0.004 waves (2 nm with 532-nm light).[12]

Compared to standard two-image NPR shearography, our data also confirm that PR shearography provides better phase discrimination, reduced speckle noise, and improved fringe contrast (Fig. 10). In our laboratory experiments, the SNR improvement is over nine decibels, though applications in natural environments may show less improvement. Future publications will detail real-world performance from airborne systems.

5 Conclusions

This paper has outlined the basic physics and mathematics of shearographic imaging, starting from first principles. Standard methods for NPR shearography and phase-stepped shearography were explained. The innovation of PR shearography was introduced and compared to the prior art. The key advantage of PR shearography versus standard NPR or PS methods is its reduced sensitivity to random speckle noise, and its ability to work asynchronously with the motions of the surface being imaged.

After outlining the shearography methods, analysis of speckle noise was presented, showing the statistical distributions of the various shearography methods. The analysis tools also can be applied to more-comprehensive computations that include other noise sources.

Finally, we showed laboratory data that confirm the efficacy of PR shearography.

Future publications will cover:

- More-comprehensive noise analyses, both analytical and from direct simulations, that include nonspeckle sources, such as photon-counting and dark noise
- First-principles simulations (laser transmitter to surface to receiver) of PR shearography, including:
    - ○ Laser coherence
    - ○ System aperture and *f/#*
    - ○ Effects of receiver and transmitter motion and rotation
    - ○ Effects of atmospheric turbulence
    - ○ Effects of polarization.
- Airborne and ground-based applications from moving systems. Ground motion of a few tens of nanometers is routinely resolved from a moving airborne platform and will be detailed in future publications.
- Operation through scattering media

6 Appendix: Derivation of Equation Eq. (62)

Equation (62) is obtained by substituting Eqs. (9) and (59)–(61), into Eq. (58)

$$\mathbf{P}(\mathbf{R_{NPR}}) = \int_0^\infty \mathrm{d}|\mathbf{E}_0| \int_0^\infty \mathrm{d}|\mathbf{E_{\Delta r}}|\mathbf{P}(\mathbf{R_{NPR}}, |\mathbf{E}_0|, |\mathbf{E_{\Delta r}}|). \tag{58}$$

First, substitute Eq. (9)

$$P(|E_S|) = 2(|E_S|/\langle I_S\rangle)\exp(-|E_S|^2/\langle I_S\rangle), \qquad 0 \le |E_S| < \infty. \tag{9}$$

Eq. (60)

$$\sin \boldsymbol{\phi}_{\text{Speckle}} = \mathbf{R_{NPR}}./(|\mathbf{E}_0|.*|\mathbf{E_{\Delta r}}|), \tag{60}$$

and Eq. (61)

$$\begin{aligned}\mathbf{P}(\sin \boldsymbol{\phi}_{\text{Speckle}}) &= \mathbf{P}(\boldsymbol{\phi}_{\text{Speckle}})(\partial\boldsymbol{\phi}_{\text{Speckle}}/\partial \sin \boldsymbol{\phi}_{\text{Speckle}}) \\ &= \frac{1}{2\pi\sqrt{1-\sin^2\boldsymbol{\phi}_{\text{Speckle}}}},\end{aligned} \tag{61}$$

into Eq. (59)

$$\begin{aligned}\mathbf{P}(\mathbf{R_{NPR}}, |\mathbf{E}_0|, |\mathbf{E_{\Delta r}}|) = \mathbf{P}(\sin \boldsymbol{\phi}_{\text{Speckle}}).*[\mathbf{P}(|\mathbf{E}_0|)./|\mathbf{E}_0|]. \\ *[\mathbf{P}(|\mathbf{E_{\Delta r}}|)./|\mathbf{E_{\Delta r}}|],\end{aligned} \tag{59}$$

to give

$$\begin{aligned}\mathbf{P}(\mathbf{R_{NPR}}, |\mathbf{E}_0|, |\mathbf{E_{\Delta r}}|) &= \frac{2}{\pi\sqrt{1-[\mathbf{R_{NPR}}./(|\mathbf{E}_0|.*|\mathbf{E_{\Delta r}}|)].^2}}. \\ &* \left(\frac{1}{\langle\mathbf{I}_0\rangle}.*\frac{1}{\langle\mathbf{I_{\Delta r}}\rangle}\right).*\exp\left(-\frac{|\mathbf{E}_0|.^2}{\langle\mathbf{I}_0\rangle}\right).*\exp\left(-\frac{|\mathbf{E_{\Delta r}}|.^2}{\langle\mathbf{I_{\Delta r}}\rangle}\right).\end{aligned} \tag{90}$$

With Eq. (90) inserted, Eq. (58) becomes

$$\begin{aligned}\mathbf{P}(\mathbf{R_{NPR}}) &= \frac{2}{\pi\langle\mathbf{I}_0\rangle.*\langle\mathbf{I_{\Delta r}}\rangle}.*\int_0^\infty \mathrm{d}|\mathbf{E}_0|.*e^{(-(|\mathbf{E}_0|.^2)./\langle\mathbf{I}_0\rangle)}. \\ &* \int_{|\mathbf{E_{\Delta r}}|=|\mathbf{R_{NPR}}|./|\mathbf{E}_0|}^\infty \mathrm{d}|\mathbf{E_{\Delta r}}|.*\frac{|\mathbf{E}_0|.*|\mathbf{E_{\Delta r}}|.*e^{(-(|\mathbf{E_{\Delta r}}|.^2)./\langle\mathbf{I_{\Delta r}}\rangle)}}{\sqrt{(|\mathbf{E}_0|.*|\mathbf{E_{\Delta r}}|).^2-\mathbf{R_{NPR}}.^2}}.\end{aligned} \tag{91}$$

Next, carry out the integral over $|\mathbf{E_{\Delta r}}|$, using the changes of variables

$$x = |\mathbf{E_{\Delta r}}|.*|\mathbf{E}_0|./\mathbf{R_{NPR}}, \tag{92}$$

and

$$y^2 = x^2 - 1, \tag{93}$$

to give

$$\begin{aligned}&\int_{|\mathbf{E_{\Delta r}}|=|\mathbf{R_{NPR}}|./|\mathbf{E}_0|}^\infty \mathrm{d}|\mathbf{E_{\Delta r}}|.*\frac{|\mathbf{E}_0|.*|\mathbf{E_{\Delta r}}|.*e^{(-|\mathbf{E_{\Delta r}}|.^2./\langle\mathbf{I_{\Delta r}}\rangle)}}{\sqrt{(|\mathbf{E}_0|^2.*|\mathbf{E_{\Delta r}}|^2)-\mathbf{R}_{\mathbf{NPR}}^2}} \\ &= \frac{|\mathbf{R_{NPR}}|}{|\mathbf{E}_0|}.*\int_{x=1}^\infty \mathrm{d}x\frac{x*e^{\left\{-\left[\left(\frac{\mathbf{R_{NPR}}}{|\mathbf{E}_0|}\right).^2\right].*\frac{x^2}{\langle\mathbf{I_{\Delta r}}\rangle}\right\}}}{\sqrt{x^2-1}} \\ &= \frac{|\mathbf{R_{NPR}}|}{|\mathbf{E}_0|}\int_{y=0}^\infty \mathrm{d}y.*e^{\left\{-\left[\left(\frac{\mathbf{R_{NPR}}}{|\mathbf{E}_0|}\right).^2\right].*\frac{(1+y^2)}{\langle\mathbf{I_{\Delta r}}\rangle}\right\}} \\ &= e^{\left\{-\left[\left(\frac{\mathbf{R_{NPR}}}{|\mathbf{E}_0|}\right).^2\right].*\frac{1}{\langle\mathbf{I_{\Delta r}}\rangle}\right\}}\frac{|\mathbf{R_{NPR}}|}{|\mathbf{E}_0|}\int_{y=0}^\infty \mathrm{d}y.*e^{\left\{-\left[\left(\frac{\mathbf{R_{NPR}}}{|\mathbf{E}_0|}\right).^2\right].*\frac{(y^2)}{\langle\mathbf{I_{\Delta r}}\rangle}\right\}}.\end{aligned} \tag{94}$$

The integral over y is just an error function so that Eq. (94) further reduces to

$$\begin{aligned}&\int_{|\mathbf{E_{\Delta r}}|=|\mathbf{R_{NPR}}|./|\mathbf{E}_0|}^\infty \mathrm{d}|\mathbf{E_{\Delta r}}|.*\frac{|\mathbf{E}_0|.*|\mathbf{E_{\Delta r}}|.*e^{(-|\mathbf{E_{\Delta r}}|.^2./\langle\mathbf{I_{\Delta r}}\rangle)}}{\sqrt{(|\mathbf{E}_0|^2.*|\mathbf{E_{\Delta r}}|^2)-\mathbf{R}_{\mathbf{NPR}}^2}} \\ &= e^{\left(-\frac{\mathbf{R_{NPR}}.^2}{\langle\mathbf{I_{\Delta r}}\rangle|\mathbf{E}_0|.^2}\right)}\sqrt{\pi\langle\mathbf{I_{\Delta r}}\rangle}\frac{1}{\sqrt{2\pi}\left[\sqrt{\frac{1}{2}\langle\mathbf{I_{\Delta r}}\rangle}./\left(\frac{\mathbf{R_{NPR}}}{|\mathbf{E}_0|}\right)\right]}\int_{y=0}^\infty \mathrm{d}y. \\ &* e^{\left(-\frac{1}{2}\frac{y^2}{\left\{\frac{1}{2}\langle\mathbf{I_{\Delta r}}\rangle./\left[\left(\frac{\mathbf{R_{NPR}}}{|\mathbf{E}_0|}\right).^2\right]\right\}}\right)} \\ &= e^{\left(-\frac{\mathbf{R_{NPR}}.^2}{\langle\mathbf{I_{\Delta r}}\rangle|\mathbf{E}_0|.^2}\right)}\frac{1}{2}\sqrt{\pi\langle\mathbf{I_{\Delta r}}\rangle}.\end{aligned} \tag{95}$$

Substituting Eq. (95) into Eq. (91) gives

$$\mathbf{P}(\mathbf{R_{NPR}}) = \frac{\sqrt{\langle \mathbf{I_{\Delta r}} \rangle}}{\sqrt{\pi}\langle \mathbf{I}_0 \rangle .* \langle \mathbf{I_{\Delta r}} \rangle} .* \int\limits_0^\infty \mathrm{d}|\mathbf{E}_0| .* e^{[-(|\mathbf{E}_0|.^2)./\langle \mathbf{I}_0 \rangle]}. \\ * e^{\left(-\frac{\mathbf{R_{NPR}}.^2}{\langle \mathbf{I_{\Delta r}} \rangle |\mathbf{E}_0|.^2}\right)}. \tag{96}$$

With the substitution $x = (|\mathbf{E}_0|/\sqrt{\langle \mathbf{I}_0 \rangle})$, Eq. (96) becomes

$$\mathbf{P}(\mathbf{R_{NPR}}) = \frac{1}{\sqrt{\pi}\sqrt{\langle \mathbf{I}_0 \rangle .* \langle \mathbf{I_{\Delta r}} \rangle}} .* \int\limits_0^\infty \mathrm{d}x. \\ * e^{\left[-x^2 - \frac{1}{x^2}\left(\frac{\mathbf{R_{NPR}}.^2}{\langle \mathbf{I}_0 \rangle .* \langle \mathbf{I_{\Delta r}} \rangle}\right)\right]}. \tag{97}$$

Finally, Eq. (97) is solvable in closed form to give[13]

$$\mathbf{P}(\mathbf{R_{NPR}}) = \frac{1}{2\pi} \frac{2\sqrt{\pi}}{\sqrt{\langle \mathbf{I}_0 \rangle} .* \sqrt{\langle \mathbf{I_{\Delta r}} \rangle}} .* \int_0^\infty \mathrm{d}x .* e^{(-x^2)}. \\ * e^{\left(-\frac{|\mathbf{R_{NPR}}|^2}{\langle \mathbf{I}_0 \rangle \langle \mathbf{I_{\Delta r}} \rangle x^2}\right)} \\ = \frac{1}{\sqrt{\langle \mathbf{I}_0 \rangle .* \langle \mathbf{I_{\Delta r}} \rangle}} .* e^{-2\frac{|\mathbf{R_{NPR}}|}{\sqrt{\langle \mathbf{I_{\Delta r}} \rangle .* \langle \mathbf{I}_0 \rangle}}}. \tag{62}$$

Acknowledgments

We gratefully acknowledge support for portions of this work from the United States Government under Contract No. W909MY-11-C-0074 awarded by the Department of the Army, and Contract No. N00014-07-C-0292 awarded by the Department of the Navy.

References

1. E. Hecht, *Optics*, 3rd ed., pp. 46–49, 368–369, Addison Wesley Longman, New York (1998).
2. J. W. Goodman, *Speckle Phenomena in Optics: Theory and Application*, pp. 10–12, 294–296, Roberts and Company, Englewood, Colorado (2007).
3. K. Creath, "Phase-shifting speckle interferometry," *Appl. Opt.* **24**, 3053–3058 (1985).
4. V. Aranchuk et al., "Pulsed spatial phase-shifting digital shearography based on a micropolarizer camera," *Opt. Eng.* **57**(2), 024109 (2018).
5. M. J. DeWeert and A. N. Acker, "Phase resolved shearography for remote sensing," US Patent 9,476,700 (2014).
6. D. Kokubun and C. E. Saxer, "Compensating aperture for utilizing shearography from a moving platform," US Patent 8,717,577 (2014).
7. C. E. Saxer, "Shearography from a moving platform," US Patent 8,804,132 (2014).
8. E. M. Louchard, "Method and system for buried land mine detection through derivative analysis of laser interferometry," US Patent 9,671,521 (2017).
9. A. N. Acker et al., "Shearogram generation algorithm for moving platform based shearography systems," US Patent 9,818,181 (2017).
10. H. A. Aebischer and S. Waldner, "A simple and effective method for filtering speckle-interferometric phase fringe patterns," *Opt. Commun.* **162**, 205–210 (1999).
11. W. K. Schomburg, *Introduction to Microsystem Design*, RWTH ed., Springer-Verlag, Berlin, Heidelberg (2011).
12. M. J. DeWeert et al., "Final report: laser interferometry system phase resolved study," Report to US Army Night Vision and Electronic Sensors Directorate (NVESD) for Contract W909MY-11-C-0074 (2012).
13. I. S. Gradsteyn and I. M. Ryzhik, *Tables of Integrals, Series, and Products, Corrected and Enlarged Edition*, Formula 3.325, Academic Press, New York (1980).

Michael J. DeWeert, PhD, is a BAE systems engineering fellow and the technical director at BAE Systems STS/EPX in Honolulu. He has over 25 years of experience in remote sensing research and development for intelligence, surveillance, and reconnaissance. His current responsibilities include technical oversight spectral imaging, LIDAR, and interferometric remote-sensing systems, and modeling and simulation for maritime and terrestrial sensing. He is also developing advanced modeling and simulation capabilities for remote sensing, interferometric imaging, and other applications.

Andrew N. Acker, PhD, is a senior principal scientist at BAE Systems in Honolulu. He has over 25 years of experience in scientific analysis and modeling and 18 years of defense industry experience in phenomenological analysis, remote sensing, and sensor and algorithm development. His recent work has focused on the development of physics and statistics-based detection algorithms, which has led to the successful implementation of real-time detection systems in both marine and terrestrial environments.

Reid Noguchi is a program manager at BAE Systems in Honolulu with over 20 years of experience in the aerospace and defense industry, particularly in the development of complex systems that incorporate leading edge, remote sensing technologies. As a program manager since 2003, he has executed contracts for mine countermeasures programs with customers from the US Navy, Marine Corps, and Army, as well as affiliated government agencies. His program activity ranges from basic research to advanced prototype development and demonstration of passive and active electro-optic remote sensing technology. Previously, he performed at BAE Systems as lead systems engineer on development and demonstration of airborne electro-optic sensor systems.

Dugan Yoon has a combined 37 years of experience in electro-optics system design, electronics circuit design, and product development. He is currently developing both active and passive EO systems for mine countermeasures. His recent activity has been focused on 2-D range gated LIDAR for underwater targets, and acoustic laser interferometry for buried targets. He has previously managed the Electrical Engineering Department, directing the development of electro-optic sensors and processing systems. Prior to BAE Systems he designed embedded electronics for transaction terminals. Prior to this, he developed detection circuits and encoder subsystems for electronic warfare receivers.

Gary Sawai has been in the high technology industry since graduating from Loyola Marymount University with a Bachelor of Science degree in electrical engineering. For the past 20 years, he has been the project manager on numerous product development programs for both military and civilian applications. The types of programs ranged from high volume point of sales terminals to redundant digital voice switching systems for air defense applications. In June 2003, he joined BAE systems as a senior systems engineer where he managed the development of various electro-optical/infrared active and passive systems. He is currently the project engineering manager (PEM) on the synoptic airborne multisensor system development program. As the PEM, he interfaces with the customer on technical issues and oversees all engineering activities on the program.